CHALMERS
UNIVERSITY OF TECHNOLOGY

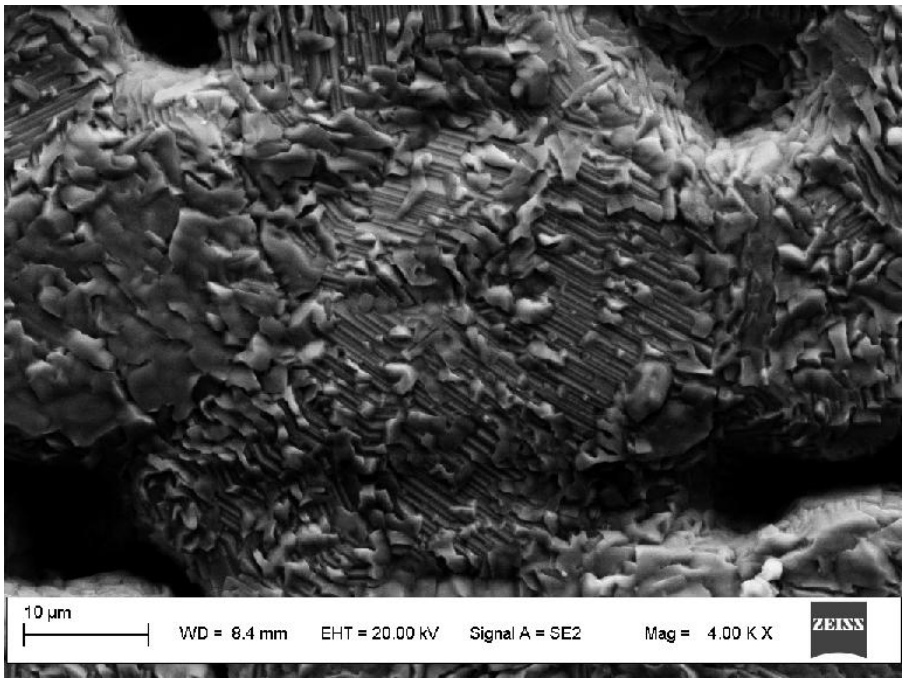

2D Nanomaterial-Reinforced Copper Matrix Composites for Tribological Applications

Master thesis in Physics

KLARA ANDERSSON

DEPARTMENT OF INDUSTRIAL MATERIAL SCIENCE
CHALMERS UNIVERSITY OF TECHNOLOGY
Gothenburg, Sweden 2026
www.chalmers.se

Abstract

Copper is widely used in electrical components, including switching devices, due to its excellent electrical conductivity. However, copper-based switching components are susceptible to friction and wear during repeated sliding contact. While oil- and grease-based lubricants can reduce friction and wear, they require maintenance, and their performance depends on operating conditions. This creates a need for low-friction, wear-resistant materials to enable efficient, reliable switching performance.

This thesis investigates whether MXene reinforcement can improve the tribological performance of copper matrix composites for electrical switching applications. MXene-Cu composites with MXene loadings ranging from 0.5 wt.% to 2.5 wt.% were fabricated and evaluated using linear reciprocating ball-on-flat measurements. The composites were characterized before and after sintering, and after tribological testing, using optical microscopy, SEM, and EDS. The MXene-Cu composites were also compared with additional material systems, namely Graphene-Cu and MXene-Graphene-Cu hybrid composites.

During the tribomechanical evaluation, the pure Cu reference was prematurely interrupted due to excessive friction. Although the measurement of one MXene-Cu composite was interrupted due to excessive friction, all other MXene-Cu composites finished the measurement. This indicates that MXene reinforcement improved sliding durability compared with pure Cu. However, the sintered MXene-Cu composites still exhibited relatively high coefficients of friction, ranging from 0.62 to 0.949, and no sustained low-friction behavior comparable to the greased reference was achieved. The 2 wt.% MXene-Cu composite showed the lowest mean coefficient of friction (CoF) among the sintered MXene-Cu samples, but the initial friction reduction was not sustained for the entire measurement. SEM and EDS analysis

suggested surface smearing and compacted wear layers, but did not confirm the formation of a continuous MXene-derived lubricating tribofilm.

Overall, MXene reinforcement showed potential for improving sliding durability, but further optimization of composition, processing, and surface condition is required before practical application in electrical switching devices can be considered.

Contents

1
Introduction

Copper is one of the most commercially used metals in production within modern industry [1]. Owing to its excellent electrical conductivity, copper is extensively used in electrical components that require electrical current to pass through such as contacts, switching devices, and connectors. However, copper possesses well-known limitations in terms of friction and wear resistance [2]. Thus, restricting the use of copper within applications that are subjected to friction, such as sliding contacts or switching devices, or mechanical loads, such as bearings. In general, the rapid development of technology and emerging technical fields have introduced more demanding requirements for conductive copper materials and push research toward novel materials and technologies forward [3].

The traditional approach to achieving low-wear and low-friction conditions has been to apply a liquid lubricant between the rubbing surfaces [4]. Another approach to improving desired properties, for example the mechanical strength or decreasing friction, is alloying the copper with small quantities of other elements, for example zinc, tin and nickel [1]. However, the alloying process introduces a trade-off between mechanical strength and conductivity as alloying significantly decreases electrical conductivity. For applications where enhancement of properties is desired without compromising on the inherent conductivity for copper, an alternative route is to introduce a reinforcement phase into the copper matrix [5]. This route allows for the copper matrix to largely retain its high electrical conductivity while the introduced reinforcement improves the mechanical and tribological properties.

MXenes are a novel 2D material derived from the bulk material MAX phase [6]. Compared to other 2D materials, such as graphene, MXenes have a larger com-

positional flexibility as they consists of a transition metal and nitrogen and/or carbon. The unique set of properties combined with a tunable surface chemistry makes MXenes a strong candidate as a reinforcement phase in copper-based matrix composites [7]. Although MXenes exhibit exceptional intrinsic properties, the final performance of the copper-based composite is strongly influenced by the reinforcement loading, the dispersion of the reinforcement phase, and the interfacial interaction between the reinforcement [8]. Poor dispersion, or even agglomeration of the reinforcement phase, may reduce the effectiveness of incorporating the reinforcement phase, and excessive loading can disrupt the continuous copper matrix and negatively affect the desired properties, such as the conductivity of the copper. Achieving a sufficiently homogeneous distribution of MXene within the copper matrix is therefore crucial when it comes to developing copper-based composites reinforced with MXene.

1.1 Purpose

The purpose of this master's thesis is to investigate whether the tribological performance of copper can be enhanced by reinforcing the copper matrix with MXene. To investigate this, MXene-Cu composites will be developed, and the tribological performance and wear-related behavior will be evaluated. Furthermore, the microstructure of the composites and the dispersion of the reinforcement phase will be investigated throughout the fabrication process and evaluation of the tribological performance. More specifically, the impact of incorporating freeze-drying in the fabrication process will be analyzed.

In addition, three different material systems will be compared: MXene-Cu composites, Graphene-Cu composites, and MXene-Graphene-Cu composites. The purpose of this comparison is to investigate which material system has the largest effect on the tribological performance, as well as to investigate any synergistic effects in the hybrid samples.

1.2 Research Question

The purpose of this master thesis can be summarized into three research questions:

1. Does incorporating MXenes into the Cu metal matrix improve the tribological properties?
2. How does incorporating freeze-drying in the processing effect the dispersion of MXene in the Cu metal matrix?
3. How does the effect of incorporating MXenes compare to the effect of other material systems, such as MXene-Graphene-Cu composites and Graphene-Cu composites?

2
Background

2.1 Electrical switching devices and sliding contacts

Electrical switching devices control the flow of electricity and are a fundamental part of electrical applications [9]. The electrical current is turned on or off by a contact that operates through physically opening or closing the circuit. Therefore, for the electrical switching device to function effectively, the contact material needs to exhibit a high electrical conductivity [10]. Apart from the demands on the electrical conductivity, the sliding motion of the electrical contact introduces issues related to friction and wear [11]. More specifically, challenges include decreasing both the wear rate and the coefficient of friction (CoF) and thereby increasing the lifetime of the contact.

2.2 Tribology of sliding contacts

The literal translation for tribology is "the science of rubbing" as the word is derived from the Greek word for rubbing, *tribos* [12]. In dictionaries, the word is more commonly defined as the science of friction, wear, and lubrication between interacting surfaces in relative motion. The science includes understanding and improving how surfaces interact in real machines, so they last longer, work better, and cost less to maintain.

2.2.1 Friction and wear

Friction is a fundamental force that resists the sliding of one surface over another. The force is always parallel to the contact surface and is directed opposite to the motion [13]. Friction arises from interaction forces between the atoms or molecules

on or near the two surfaces that are in contact. The interaction forces can be described as forces of adhesion, which are similar to electronic bonding forces. The more strongly the atoms on one surface attract those on the other surface, the greater the friction force between the two surfaces. At the contact surface of sliding objects, friction is considered a dissipative force, meaning it turns energy into heat. Under these circumstances, additional energy is required apart from the energy needed to accomplish the desired objective [13]. While the frictional force transforms most of the excess energy into heat, a smaller fraction contributes to surface degradation and material removal, commonly referred to as wear.

2.2.2 Wear mechanisms

Wear is defined as the progressive removal of surface material due to friction [14]. Despite the quantities of material being removed by wear being quite small, the degrading mechanisms are often considered one of the main reasons for failure in many mechanical parts. The two most common types of wear are abrasive and adhesive wear [15]. Abrasive wear occurs when a harder surface slides across a softer surface [16]. The harder surface will then dig into the softer surface and plow a series of grooves. The material originating from the grooves is normally removed as debris. If the generated debris is hard enough, it may, in turn, cause additional abrasive wear. Adhesive wear, on the other hand, is caused by attractive forces between the surface atoms of the two materials subject to sliding motion [16]. Due to the attractive forces, material will get pulled from one surface and transfer onto the other. The removed material is commonly referred to as an adhesive wear fragment.

Two additional relevant mechanisms are plastic deformation and delamination. Plastic deformation occurs because nominally flat metal surfaces are not truly planar but are instead covered with asperities [17]. When two metal surfaces come into contact, only a few asperities make contact, resulting in a real contact area that is much smaller than the apparent area. As the surfaces are brought together, the asperities are flattened through plastic deformation, which increases the real contact area. As these asperities deform during plastic deformation, repeated loading

can generate cracks beneath or near the surface [18]. Once nucleated, these cracks propagate as the load continues, causing material to detach as pits or flakes. The detached fragments may then act as third-body abrasive particles, leading to the formation of additional grooves.

Although there is no simple, universal relationship between friction and wear, changes in friction can influence the wear process by altering the contact conditions, surface damage, and amount of energy dissipated during sliding [14]. One example of a mechanism that is related to this is plastic deformation. Plastic deformations contribute to wear and friction simultaneously by redistributing or removing material, while influencing friction as the deformation dissipates energy and affects the real contact area between the sliding surfaces.

2.2.3 Evaluation of friction and wear

A commonly used method for evaluating friction and sliding wear is the linear reciprocating ball-on-flat measurement [19]. The main idea is that a normal load is applied on a spherical counter body that is brought into contact with a flat sample. The flat sample then moves back and forth along a straight path, creating a linear reciprocating motion. During the test, the frictional force is measured and, in turn, used to determine the CoF. After the test, data related to how the CoF evolves during sliding distance or cycles can be obtained. As well as the mean CoF. Test parameters that can be varied include the sliding velocity, normal load, and wear track length.

The tribomechanical test results in a wear track on the flat sample, which can be analyzed after the test to assess wear morphology and potential wear mechanisms. To quantify the amount of wear damage done to the flat specimen, the volume of the removed material is commonly used [20]. However, the wear track width may be used as an indication of the wear damage to the specimen if the samples were compared under similar test conditions [21], [22]. In this case, a broader wear track may indicate larger wear, while a reduction in wear track may indicate improved

wear resistance.

Although all previously discussed wear mechanisms most likely occur simultaneously, analyzing the wear track using Scanning Electron Microscopy (SEM) can give an indication of what wear mechanism dominated the wear damage in that particular site [23]. Indications of abrasive wear are long, parallel, straight grooves in the wear track. Figure 2.1a shows a representative SEM image of how abrasive wear may manifest on a sample surface. In addition, Figure 2.1a shows how delamination wear may manifest on a sample surface. Adhesive wear is recognized by material adhering to the body's surface. To provide additional proof of adhesion on the substrate surface, additional chemical analyses, such as EDS, can be performed. Figure 2.1c shows a representative SEM image of how abrasive wear may manifest on a sample surface. Dark surface regions in SEM images may indicate compositional or chemical differences compared with the surrounding metallic surface. Figure 2.1b shows a representative SEM image of how chemically modified surface regions may appear on a worn surface.

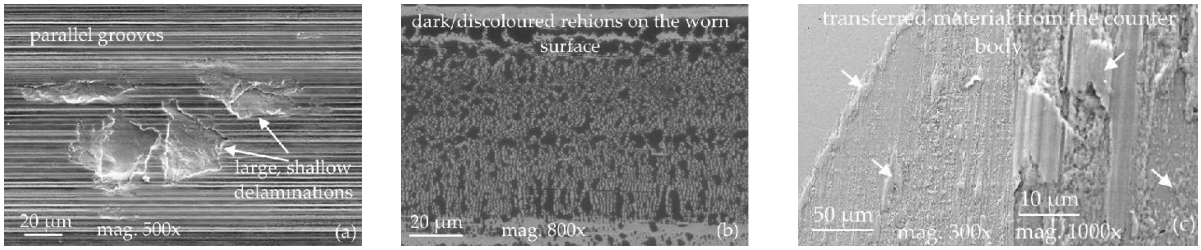

(a) Representative SEM image of abrasive wear on a metallic surface.

(b) Representative SEM image of abrasive wear on a metallic surface.

(c) Representative SEM image of adhesive wear on a metallic surface.

Figure 2.1: Representative SEM images of wear appearances associated with (a) abrasion, (b) chemical reactions and (c) material transfer by adhesion. Adapted from Sieberg et al. [23], licensed under CC BY 4.0.

2.2.4 Lubrication and friction reduction

The traditional approach to achieving low-wear and low-friction conditions has been to apply an external lubricant between the rubbing surfaces [4]. The lubricant separates the rubbing surfaces by introducing a low-shear, high-durability boundary film between them and thus avoiding metal-to-metal contact. Lubricants typically

consist of oil or grease. One property that largely determines the performance of a lubricated contact is viscosity [15]. Although the viscosity within the lubricant provides resistance during shear, the idea is that the viscous resistance is much smaller than the frictional resistance during dry sliding. One issue with the traditional liquid lubricants is the sensitivity to harsh environments, as the flow characteristics of the liquid lubricant may be affected by temperature [24]. More specifically, if the temperature drops below the pour point, the lubricant may no longer flow sufficiently to the contact surfaces. Another issue with external lubrication is that it requires regular maintenance, in terms of oil changes and re-greasing [25]. Introducing operational costs as an additional issue with relying on external lubrication.

Another driver to moving away from external lubrication is to increase energy efficiency [26]. Currently, approximately 20 % of all the world's total energy consumption goes to overcoming friction. Furthermore, it's estimated that 8.7 % of the energy spent on friction could be saved due to advancements in new materials, lubricants, and design changes.

An alternative approach to external lubrication is the use of solid lubricants, either as a surface coating or as reinforcement phases in a composite material [27]. Solid lubrication is most commonly used in applications where liquid lubricants are unsuitable, for example, due to operating conditions, environmental restrictions, or maintenance requirements. Just like the external lubricant, the solid lubricants can reduce friction and wear by forming low-shear layers between the contacting surfaces, thereby limiting direct metal-to-metal contact.

2.3 Copper for electrical contact applications

Due to the high electrical conductivity and formability, copper is used extensively for electrical contacts and other current-carrying components [28]. However, copper has well-known limitations when it comes to both wear resistance and mechanical strength, limiting its performance in applications subjected to friction, such as a sliding contact [2]. Thus, when it comes to using copper for electrical contact appli-

cations, the desired conductivity and formability has to be balanced with limitations in tribological properties.

2.3.1 Relevant properties of copper

After silver, copper is the next best conductor of electricity [28]. Furthermore, copper is a highly ductile metal, thanks to its face-centered cubic (FCC) crystal structure, which enables extensive plastic deformation before fracture [29]. Copper's malleability allows it to be formed and processed into unique shapes and sizes [28]. In addition, copper is abundant, cost-effective, and easy to refine, contributing to its widespread use in current-carrying components [29].

However, the same ductility and relatively low hardness that contribute to copper's formability [30] also make it susceptible to plastic deformation during sliding contact, which can limit its wear resistance [31]. Based on mechanical tests performed on metallic materials, it has been observed that strength and ductility are mutually exclusive properties [32]. This results in copper's well-known limitations in terms of its mechanical strength and wear resistance [2]. These limitations become especially relevant in sliding contacts, where local asperity interactions can lead to plastic deformation, adhesion, material transfer, and increased friction [33] [30].

2.3.2 Limitations of copper in sliding contact

During sliding contact, the real contact between the surfaces occurs at asperities [33]. The frictional characteristic of the sliding surfaces is heavily dependent on how the asperities interact. Due to the small real contact area, the local stresses can become high, which may cause plastic deformation, flattening, smearing, and material transfer at the surface. Apart from plastic deformation at the contact, copper is also affected by adhesion [33]. Adhesion stems from molecular and atomic bonds that are broken and formed at the surface interface during sliding. However, when asperities come in contact, growing junctions can be formed. The junction grows as more atoms bond to each other. As this adhered junction stretches along the sliding direction, plastic deformation and material transfer could be observed. For materi-

als where adhesion dominated the sliding process, such as copper, higher coefficients of friction can be observed.

2.3.3 Strategies for improving copper

Three common approaches for improving copper are alloying, surface coatings, external lubrication, and incorporating reinforcement phases.

One common approach to improving the strength, hardness, or wear resistance of copper is alloying the copper with small quantities of other elements, for example, zinc, tin, and nickel [1]. However, the alloying process introduces a trade-off between mechanical strength and conductivity as alloying can reduce the electrical conductivity.

A second approach to specifically enhance the tribological properties of copper is to modify the copper surface by adding a coating on the copper substrate [34]. The efficiency and effectiveness of the coating on the tribological performance depend heavily on the quality of the coating, including its homogeneity and thickness, and how well the coating adheres to the substrate. As previously mentioned, the external lubrication acts as a boundary film between the two rubbing surfaces [4].

A third way to improve the mechanical and tribological properties of copper is through copper matrix composites. In this approach, copper serves as a ductile matrix into which reinforcement particles are introduced [35]. In contrast to alloying, the resulting copper matrix composite allows for the composite to largely retain its high electrical conductivity while the introduced reinforcement enhances the mechanical and tribological properties [5].

2.4 Copper matrix composites

As the requirements on copper-based components become increasingly demanding, strategies for improving the properties of copper are of growing interest [5]. To enhance the mechanical and tribological performance while retaining the conduc-

tivity, copper matrix composites have attracted attention as a potential route. The conductivity can potentially be largely retained because the copper matrix remains continuous. The copper matrix composites are then formed by introducing one or more reinforcement phases with desirable properties into the continuous copper matrix. Researchers have targeted the enhancement of mechanical properties, such as strength and fracture toughness, of copper using copper-based composites [5]. An additional targeted enhancement through copper-based composites is the tribological properties.

Through copper-based composites, the intrinsic mechanical and tribological properties of copper may be enhanced, resulting in composites with friction-reducing and anti-wear properties [36].

2.4.1 Reinforcement phases in copper

To increase the strength of the copper composite, the introduced reinforcement phase has to be stiffer than the copper [5]. When a load is applied, the load can then be transferred from the soft copper to the reinforcement phase. The efficiency of the load transfer depends on how strong the interaction between the copper and the reinforcement phase is. A weak interaction might cause the reinforcement to act as a defect in the composite instead of increasing the strength. In addition to load transfer, introducing a harder or stiffer reinforcement phase into the copper matrix may cause an increase in observed yield strength due to increased dislocation blocking and a reduced copper grain growth [37]. Where dislocations previously would move freely through the copper matrix during deformation, the reinforcement phase acts as an obstacle. Obstacles lead to an increase in stress required for further plastic deformation, which, in turn, leads to a stronger and stiffer material. The reinforcement material also hinders the growth of grains during sintering [5]. Smaller grains are generally related to an increased strength in the material [37]. Increasing the strength of the composite by introducing a harder reinforcement might also lead to increased wear resistance due to less plastic deformation and material removal [5]. In addition, reinforcing copper with materials exhibiting inherent lubricating

properties, solid lubricants, can enhance the tribological properties of the copper matrix composite [38]. By introducing a solid lubricant into the copper matrix, a self-lubricating composite can be formed. The self-lubricating properties stem from the formation of a boundary layer during sliding with lubrication provided by the solid lubricant. The lubricating boundary layer reduces the direct contact and facilitates smooth interaction at the sliding interface. In addition, during friction activities, the solid lubricant that was previously embedded in the composite may be released [38]. This enables a continuously replenished lubricating boundary film at the sliding contact.

2.4.2 Challenges in copper-based composite fabrication

The reinforcement material, its concentration, and the fabrication process influence the microstructure of the copper matrix composite [38]. Three relevant challenges in composite fabrication include achieving a homogeneous dispersion of reinforcement phase in the copper composite, strong interfacial interactions, and finding an appropriate reinforcement loading [38].

One important parameter is the dispersion of the reinforcement material within the copper matrix. as it affects how efficiently the reinforcement material enhances the desired properties [38]. To exemplify, the dispersion affects the porosity and grain development in the composites. In addition, at higher reinforcement loadings, higher porosity and increased agglomeration of reinforcement material are more commonly observed [38]. If the reinforcement phase is agglomerated or there is poor interfacial bonding, the effectiveness of the reinforcement may be reduced. Balancing the reinforcement loading is important because too low loading might not enhance the desired properties sufficiently, but too high reinforcement loading may disrupt the copper matrix and therefore reduce the conductivity [38]. To enhance the interfacial bonding between the copper and the reinforcement phase and the overall performance of the composite, a well-dispersed reinforcement phase is fundamental. The dispersion and the interfacial interactions are influenced by the

composite processing technique [8].

2.5 Two-dimensional reinforcement materials

Due to their exceptional intrinsic properties, two-dimensional nanomaterials have gained significant attention as reinforcement phases in composite materials [39]. Two nanomaterials with the potential to enhance both the mechanical and tribological properties of the composite are graphene and its derivatives, and MXenes.

2.5.1 Graphene

Graphene is derived from the bulk material graphite, resulting in a material consisting of a single layer of carbon atoms arranged in a honeycomb lattice [40]. The strong bonds between the carbon atoms in the lattice make graphene one of the strongest materials to date, with a measured strength corresponding to a Young's modulus of 1 TPa for defect-free graphene sheets [4]. In addition to its remarkable mechanical strength, graphene exhibits promising tribological properties due to the low shear resistance between its sheets [41]. The low shear resistance is commonly attributed to weak van der Waals interactions between graphene layers. This means that the graphene layers can slide easily past each other. While graphene has promising properties, processability issues arise when it comes to achieving strong interfacial bonding and a homogeneous distribution of graphene in the copper matrix [42]. Among other reasons, these issues may stem from the chemically inert graphene surface, aggregation of graphene layers due to van der Waals interactions, and poor wettability. By using graphene derivatives, such as graphene oxide (GO) or reduced graphene oxide (rGO), some issues regarding the processability can be improved [41]. The derivatives contain oxygen functional groups, which introduce more chemistry to the inert graphene surface, making the surface more polar and chemically reactive. This increases the dispersibility as there are additional forces acting on the 2D sheets, apart from the attractive van der Waals attractions. However, oxidizing the graphene to derive GO (and then potentially reducing it to derive rGO) disrupts the perfect graphene structure, and the exceptional strength and conductivity observed in graphene may be compromised. Hence, a trade-off between

maintaining attractive properties and good processability may emerge.

2.5.2 MXenes

Another nanomaterial with potential to enhance both the mechanical and tribological properties of copper-based composites is MXenes [39].

First synthesized in 2011, MXenes are a family of 2D transition metal carbides, nitrides, and carbonitrides [6]. The name MXene originates from the components of their precursor materials, the layered MAX phases, combined with the suffix "-ene" to highlight their structural similarity to graphene. One of the most widely investigated MXenes is the titanium carbide $Ti_3C_2T_x$, which is typically derived from the MAX phase Ti_3AlC_2.

2.5.2.1 MAX phases and MXene synthesis

MAX phases are a family of layered ternary carbide and nitride materials [43]. Many of these compounds were first synthesized in the 1960s by Nowotny and co-workers, who reported a large number of previously unknown ternary carbides and nitrides. However, the concept of MAX phases as a distinct material class was established later, in the 1990s, through the work of Barsoum and co-workers. Today, more than 300 MAX phases have been identified. The MAX phase consists of a transition metal "M", an A group element "A", and carbon and/or nitrogen, X, forming the structure $M_{n+1}AX_n$, where n = 1,2 or 3 [44]. The crystal structure of the MAX phase is hexagonal and consists of M-X layers interleaved with A atomic layers. While the M-X bonds are exceptionally strong due to the mixed metallic–covalent bonding, the M-A bonds are relatively weak.

MAX phases exhibit dual metallic-ceramic properties [45]. The ceramic-like traits stem from the strong M-X bonds, leading to high stiffness, high thermal stability, and melting points, and chemical stability. However, unlike other materials with ceramic properties, MAX phases exhibit metallic properties simultaneously. This

occurs because the transition metal, M, present in the compound provides delocalized electrons that can move through the structure, leading to good electrical and thermal conductivity.

The weaker M-A bonds found in the MAX phases make it possible to exfoliate the 2D material MXene from the 3D precursor MAX phase [45]. MXenes are commonly derived from the 3D precursor material MAX phase through a top-down fabrication process [6]. This is done by selectively etching away the "A group" element and replacing it with surface termination groups. Leaving a layered $M_{n+1}X_nT_x$ structure with surface terminations denoted T_x.

The weaker M-A bonds causes them to be the more reactive species in the MAX phase compound [6]. To exfoliate $Ti_3C_2T_x$ from Ti_3AlC_2 the aluminum can be selectively etched away through wet-chemical etching in hydrofluoric acid (HF), as the fluoride and aluminum species form soluble aluminum fluoride complexes. Thus, dissolving the aluminum and leaving a M-X structure, according to the following reaction:

$$Ti_3AlC_2 + 3HF \Rightarrow Ti_3C_2 + AlF_3 + 3/2H_2 \tag{2.1}$$

During etching with HF, the replacement surface terminations arise from reactions between the exposed reactive transition metal, M, and the elements present in the etching solvent [6]. As the etching solvent consists of water and fluoride complexes, the surface terminations are commonly hydroxyl and/or fluoride groups, according to Reaction 2.2 and 2.3.

$$Ti_3C_2 + 2H_2O \Rightarrow Ti_3C2(OH)_2 + H_2 \tag{2.2}$$

$$Ti_3C_2 + 2HF \Rightarrow Ti_3C2F_2 + H_2 \tag{2.3}$$

Viewing reaction 2.2 and 2.3 as separate reactions is a simplification, as it seems like the surface terminations are either -OH or -F. In reality, it's most likely a combination of the reactions, resulting in both surface termination groups. Therefore,

T_x is generally used to denote all possible surface terminations. However, exfoliating MXenes from the MAX phase using HF-etching requires multiple processing steps, as separate steps for etching, washing, and delamination of the MXene sheets are needed [46]. In addition, delamination, the separation of the MXene sheets, is dependent on the addition of an intercalant to expand the distance between the sheets. Apart from being a laborious process, HF-etching also requires the use of concentrated HF, which is highly corrosive and toxic.

An alternative route to using concentrated HF for the etching process is by generating the HF in-situ by combining hydrochloric acid, HCl, and fluoride salts such as LiF, both abundant and low-cost chemicals [46]. By letting the LiF dissolve in a HCl and distilled water solution, HF can form during the reaction according to the following reaction:

$$LiF + HCl \Rightarrow HF + LiCl \tag{2.4}$$

Once the HF has formed, Reaction 2.1, 2.2 and 2.3 can occur. The route also allows for synthesizing MXenes in a one-step procedure as etching and delamination of the MXene sheets occurs simultaneously [46]. While the fluoride species in the fluoride salt dissolves the aluminum, leaving the layered $M_{n+1}X_nT_x$ structure, the cation can intercalate between the $M_{n+1}X_n$ layers. The intercalation helps delamination and modifies the material properties of the MXene sheets. Thus, using this method, large fractions of single-layered MXene flakes with high yields, large lateral sizes, and good quality can be readily produced [46].

2.5.2.2 Properties of MXenes

Since their discovery, MXenes have emerged as a distinct group of 2D materials due to their unique combination of properties [47]. MXenes exhibit a high electrical and thermal conductivity, excellent mechanical strength, and good stability at higher temperatures. Furthermore, MXenes combine metallic conductivity, large surface area, and tunable chemistry, making them suitable for a wide range of applications [47]. To accommodate the different applications, the properties of MXene

can be tuned by varying the elements constituting the M and X layers.

Similar to graphene, MXenes exhibit a unique combination of properties by demonstrating high electrical and thermal conductivity and excellent mechanical strength [47]. When deriving MXenes from the MAX phase, surface functionalities are commonly introduced on the surfaces of the MXene sheets. These surface functionalities set MXenes apart from graphene, as more surface chemistry is an intrinsic property. The more complex structure of MXene can be attributed to the fact that it contains more than one element [6]. A more complex structure that contains more than one element may offer the possibility of tuning to achieve specific properties due to a larger compositional flexibility.

2.5.2.3 MXenes as reinforcement phases

MXenes are a strong candidate as a reinforcement phase in metal matrix composites, due to the unique set of properties, previously described, combined with a tunable surface chemistry [7].

When introducing MXenes as a reinforcement phase in copper matrix composites, the high in-plane mechanical stiffness of the MXene sheets may contribute to enhancing the mechanical properties through increasing the load-bearing capacity, restricting plastic deformation, and hindering dislocation motion in the copper matrix [5] [48]. The hardness and wear resistance of the composite may improve if the reinforcement phase is well dispersed and the strength of the interaction between copper and MXene [5].

The two-dimensional structure leads to a high surface-to-volume ratio. In turn, this leads to better adhesion and stronger interaction with the copper matrix [39]. The van der Waals interactions holding together the MXene sheets might cause the sheets to restack or even agglomerate [49]. If the MXene sheets agglomerate, they are not well-dispersed within the copper matrix. Restacking or agglomeration may also reduce the active surface area, causing weaker interactions between the copper

matrix and the MXene. Overall, restacking or agglomeration of MXene sheets reduces the reinforcing effect.

Furthermore, MXenes have shown potential as a reinforcement phase in copper-based composites, for improving the tribological properties [48].

2.5.2.4 Lubricating mechanisms of MXenes

The enhancement of tribological properties resulting from the incorporation of MXenes into a metal matrix composite can be attributed to the formation of tribolayers, the easy-shear ability, and sliding-induced graphitization [50]. The tribofilm is a self-organized surface layer that forms at the interface of sliding materials under mechanical and thermal stress, driven by tribochemical reactions. It acts as a "third body," meaning that it is neither the original material nor the external lubricant, but rather a dynamically evolving layer that accommodates shear during sliding. The tribofilm typically consists of oxide species originating from the substrate and/or counterbody, which are intermixed with chemically and structurally degraded MXene nanosheets formed during sliding [34].

To better understand the tribofilm, spectroscopic instruments, such as energy-dispersive X-ray spectroscopy (EDS), have been extensively used on the worn surface after tribomechanical measurement. Jia et al. investigated copper matrix composites reinforced with different amounts of the MXene $Ti_3C_2T_x$ [51]. After the frictional experiments, EDS analysis was performed on the worn composite surface to verify the elemental composition and the spatial distribution on the surface. The EDS analyses on the worn Cu-$Ti_3C_2T_x$ composite surface showed a uniform distribution of Cu, Ti, C, and O. The presence of Ti indicates the formation of a continuous tribofilm with MXene spread across the contact area. The tribomechanical measurement was performed with an iron counter body. Furthermore, it was observed that the Fe content decreased with increasing $Ti_3C_2T_x$ content and disappeared at 15 wt.%. This suggests that material transfer from the counter body was suppressed due to the formation of an MXene-derived lubricating layer.

The formation of a tribolayer can reduce friction and wear by limiting direct contact between the sliding surfaces. In addition, the tribolayer can reduce the plastic deformation beneath the surface from repeated sliding [50]. More specifically, the formation of an MXene-rich tribofilm helps reduce friction and wear due to the easy-shear property of MXene [52]. The MXene sheets are able to slide under low shear forces due to the weak van der Waals interactions between them. Additionally, the strong in-plane bonds allow the sheets to stay intact and move easily without separating. A similar mechanism is observed for graphitic carbon, where the layered structure and weak interlayer interactions enable low-shear sliding. While the tribolayer reduces friction and wear, the layer itself is assumed to be constantly consumed during sliding [50]. However, the tribolayer is also assumed to be regenerated as fresh solid lubricant material reaches the surface during wear. Therefore, the tribolayer stays intact as long as there is a dynamic equilibrium between consumption and regeneration of the tribolayer.

Sliding-induced graphitization is another, previously mentioned, mechanism that contributes to the enhancement of tribological properties when incorporating MXenes [50]. The graphitic carbon structures stem from the reorganization of carbon species present at the contact surface during sliding. The carbon species arise from the decomposition of the MXenes due to mechanical strain and tribochemical reactions at the contact surface. The graphitic carbon formed during the graphitization is beneficial for enhancing the tribological properties because the film provides solid lubrication and prevents direct contact between surfaces [53]. If the graphitic carbon is approaching the structure of graphene, by consisting of a few or single layers, it's especially lubricating [41]. Similar to MXene, the graphene layers are held together by weak van der Waals forces, providing easy-shear and therefore excellent self-lubricating properties. Graphene may be considered a more efficient solid lubricant than MXene as the surface terminations on the MXene sheets form bonds during sliding [54].

2.6 Processing of powder-based copper composites

The most widely used method to prepare copper matrix composites is powder metallurgy, where the fabrication relies on blending the reinforcement phase with the powder metal matrix [5] [55]. After uniform mixing is achieved, the powder is compacted to a solid green body [5]. The green body is then sintered at a high temperature. One of the main benefits of powder technology is the increased control of the distribution of the reinforcement material in the copper matrix.

2.6.1 Powder mixing and dispersion

First, the metal matrix powder and the reinforcement phase must be mixed to achieve a suitable distribution before compaction and sintering [56]. This step is important because the distribution of the reinforcement phase influences the final microstructure and, therefore, the mechanical and tribological properties of the composite.

Powder mixing can be performed by blending dry powders or by dispersing the powders in a liquid, often referred to as wet or slurry-based mixing [48]. For MXenes, slurry-based processing is particularly relevant as the surface terminations introduced during etching give MXene sheets a negative surface charge. The surface charge contributes to the solution-processibility of MXenes and makes them suitable for liquid-based mixing methods. Therefore, MXenes exhibit good compatibility with solution-based processing routes for metal matrix composites, in addition to their conductivity and mechanical strength [48].

After slurry-based mixing, the liquid must be removed without disrupting the particle distribution [57]. One approach for this is freeze-drying.

2.6.2 Freeze-drying

Freeze-drying can be used to produce a dehydrated powder from a wet mixture [58, 59]. First, the wet mixture is frozen, for example by placing it in a cold bath [58]. To achieve rapid freezing, liquid nitrogen can be used as the cooling medium. Rapid freezing can help preserve the particle distribution within the composite mixture, as the diffusion dynamics are insufficient to induce significant particle movement [60]. In addition, rapid freezing may reduce density-driven segregation by limiting the time available for the copper particles to separate before the particle distribution is frozen in place [61]. The frozen sample is subsequently placed in a freeze-dryer, where the solvent is removed by sublimation. During sublimation, the solvent transitions directly from solid to gas [58].

A further potential advantage of freeze-drying is that it may reduce drying-induced agglomeration compared with evaporation-based drying [62, 63]. Capillary forces can develop during conventional drying and pull the particles together. These forces promote aggregation of the particles. In freeze-drying, on the other hand, the solvent is removed through sublimation instead of evaporation. This may limit capillary-force-driven shrinkage and particle rearrangement during drying.

The full freeze-drying process results in a dehydrated composite powder that may retain the spatial distribution of the particles present in the frozen mixture [59, 60].

2.6.3 Cold pressing

In cold pressing, loose powder is compacted in a die to form a green body [64]. During compaction a green body forms due to rearrangement and deformation of powder particles at their contact points. The green body does not exhibit full metallurgical bonding but increased particle-particle contact, compared to the composite powder.

The metallurgical bonding occurs in the following sintering step where metallic bonding is promoted between the particles though neck formation and mass transport

[65].

2.6.4 Sintering

Sintering is the process of consolidating the green body through the application of heat [66]. The sintering process strongly influences the properties and performance of the sintered product by affecting microstructural features such as grain size, porosity, and grain boundary morphology [67]. During the sintering process, the structure recrystallizes, and particles diffuse across particle contacts [66]. As diffusion is extremely slow for solid powders at room temperature, sintering is performed at elevated temperatures [67]. However, the sintering temperature is generally kept below the melting temperature to avoid complete melting or unwanted phase changes.

During sintering, necks form at the contact points between adjacent powder particles [66]. As sintering continues, the composite densifies previously separated particles gradually bond into a consolidated structure. When the atoms diffuse across the particle contacts, the necks will grow and therefore increase the bonding between the particles.

3
Method

The laboratory work consisted of four main parts: synthesizing the MXene Ti_3C2 from the MAX phase Ti_3AlC_2, fabricating the MXene-Cu and graphene-containing composites, performing tribo-mechanical tests on the composites, and characterizing the microstructure of the samples. The main materials used in this work were Ti_3AlC_2 MAX phase powder, hydrochloric acid, lithium fluoride, copper powder, graphene oxide, and distilled water.

3.1 MXene Synthesis

30 mL of hydrochloric acid (HCl) was added to 10 mL of distilled water in a plastic bottle. Subsequently, 3.2 g of lithium fluoride (LiF) was added. The mixture was stirred with a magnetic stirrer to dissolve the salt. 2 g of Ti_3AlC_2 MAX phase powder was added in small increments over 10 min to control the exothermic reaction and reduce excessive gas formation. The mixture was left for 24 h on the magnetic stirrer with the lid placed, but not secured, on top of the plastic bottle.

After the 24 hours, the mixture was distributed into centrifugal tubes to enable washing with distilled water via centrifugation. First, an MPW-352 centrifuge was used at 3500 rpm for 5 min. Following each centrifugal cycle, the supernatant was discarded and replaced with fresh distilled water. This process was repeated until the pH value reached 5 and the supernatant turned greenish/black, commonly 5 to 6 cycles. The initial exfoliation process consisted of alternating light sonication for 10 s and hand shaking for 10 s. This process was repeated three to four times. Before moving on to collecting the MXene sheets, the mixture was vortex-mixed for shorter intervals, 5 s. This was repeated four to five times per centrifugal tube.

To collect the exfoliated MXene sheets, the MPW-352 centrifuge was set to 2000 rpm for 5 min. This caused the heavier components, such as unexfoliated particles, multilayer MXene, or residual MAX phase, to sink and allowed for the lighter, exfoliated sheets to be collected as a MXene dispersion through the supernatant. The centrifuge tubes were then refilled with distilled water, and the sediment was re-dispersed. The collection process was repeated five times. To go from a MXene-distilled water solution to a MXene paste, the solution was centrifuged in the MPW-352 centrifuge at 10 000 rpm for 20 min. While the MXene flakes precipitated at the bottom of the centrifuge tube, the supernatant could be discarded. This resulted in a paste-like consistency.

The MXene concentration of the resulting paste was determined by weighing a small portion of the paste before and after it was placed in a vacuum oven at 40 °C for 20 h. The MXene concentration in the first four produced pastes ranged from 42 to 44 wt.% MXene. A mean of 43 wt.% MXene was used.

3.2 Composite Fabrication

Two different groups of composites were fabricated: MXene-Cu composites and graphene-containing composites. See Table 3.1 and 3.2 for each composition and batch masses used.

MXene content [wt.%]	Total mass [g]	Cu mass [g]	Pure MXene mass [g]	MXene paste mass [g]
0.5	4.00	3.98	0.02	0.0465
1.0	4.00	3.96	0.04	0.0930
2.0	4.00	3.92	0.08	0.1860
2.5	4.00	3.90	0.10	0.2330

Table 3.1: Compositions and batch masses used for the fabrication of MXene-Cu composites.

MXene content [wt.%]	GO content [wt.%]	Total mass [g]	Cu mass [g]	GO mass [g]	Pure MXene mass [g]	MXene paste mass [g]
0.25	0.25	4.00	3.98	0.01	0.01	0.0230
0.5	0.5	4.00	3.96	0.02	0.02	0.0465
1.0	1.0	4.00	3.92	0.04	0.04	0.0930
0	0.5	4.00	3.98	0.02	–	–
0	1.0	4.00	3.96	0.04	–	–
0	2.0	4.00	3.92	0.08	–	–

Table 3.2: Compositions and batch masses used for the fabrication of graphene-containing copper composites.

3.2.1 Preparation of MXene-Cu Composites

Before adding the MXene paste, the copper was weighed out in a fume hood to minimize airborne powder exposure. Each composite mixture was initially mixed with a few drops of distilled water using a fine needle to form a viscous composite slurry inside the fume hood. See Figure 3.1.

Figure 3.1: Premixed MXene-Cu composite slurry. Mixed with a needle.

To further mix the composite slurry, a planetary mixer was used 3.2a. Table 3.3 describes the performed scheme. Between the rounds, the composite mixture rested around 1 min.

	rpm	Time [min]	Type
Round 1	1800	2	Mixing
Round 2	2000	2	Mixing
Round 3	2000	2	Mixing
Round 4	1200	0.75	Degass

Table 3.3: Planetary mixer scheme used for composite slurry preparation, including rotational speed, time, and mixing mode.

(a) Planetary mixer used for slurry preparation.

(b) MXene-Cu composite slurry after planetary mixing.

Figure 3.2: Planetary mixer and resulting MXene-Cu composite slurry after the mixing scheme.

3.2.2 Preparation of Graphene-Containing Composites

For the graphene-containing composites, the same slurry-based fabrication route was used as for the MXene-Cu composites. Instead of MXene, a commercial graphene oxide powder was used. To disperse the GO powder with the copper particles, a few drops of distilled water was added to form a viscous composite paste. As the MXene paste naturally consisted of approximately 57 wt.% distilled water, more drops of distilled water had to be added to the GO-Cu powder mixture then the MXene-Cu slurry to achieve the same viscosity.

3.2.3 Freeze-Drying

To remove the water present in the composite mixtures, the samples were frozen using liquid nitrogen (See Figure 3.3a) and then freeze-dried for 48 h (See Figure 3.3b.

(a) Composite mixture in an Eppendorf tube during freezing in liquid nitrogen.

(b) Freeze-dryer used to remove the frozen solvent by sublimation.

Figure 3.3: Freeze-drying procedure, showing (a) freezing of the composite mixture in liquid nitrogen and (b) the freeze-dryer used for solvent removal.

Depending on the water content of the MXene-Cu composite slurry, the results were either a MXene-Cu composite powder (See Figure 3.4a), a compact MXene-Cu composite or a combination of the two (See Figure 3.4) after the present water had sublimated in the freeze-dryer. To turn the compact composite into a composite powder, it had to be crushed gently using a spoon in a Petri dish.

(a) Freeze-dried MXene-Cu composite powder.

(b) A combination of compact MXene-Cu composites and MXene-Cu composite powder after freeze-drying.

Figure 3.4: Different forms of MXene-Cu composite material obtained after freeze-drying: (a) composite powder and (b) including compact MXene-Cu composites.

3.2.4 Cold Pressing

The composite powder could then be turned into a green body through cold pressing in a hydraulic press (See Figure 3.6) using an applied load of approximately 10 t (See Figure 3.5b). To ensure a uniform sample size, the composite powder was pressed in a circular steel mold with a diameter of 9 mm. Resulting in cylindrical samples with the same diameter and a height dependent on the amount of composite powder (see Figure 3.5c).

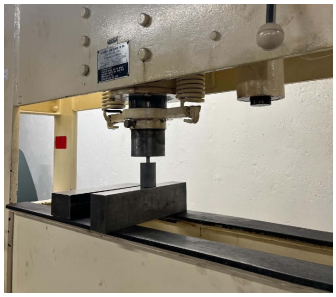

(a) Hydraulic press setup used for cold pressing.

(b) Applied load of approximately 10 tonnes.

(c) Pressed composite samples after cold pressing.

Figure 3.5: Cold pressing of the composite powders, showing (a) the hydraulic press setup, (b) the applied load, and (c) the resulting pressed composite samples.

3.2.5 Sintering

The green bodies were then consolidated through conventional furnace sintering (See Figure **??**). The program cycle consisted of three segments. The first segment included heating the furnace to a set target temperature of 1050 °C, with a heating rate of 10 °C per minute. After heating, the second segment included a dwell time of 1 h at 1050 °C. The third and final segment consisted of a reset segment to allow the furnace to cool down before taking the samples out. The full cycle used a continuous flow of argon gas to create an inert environment. At 100 °C the gas could be turned off.

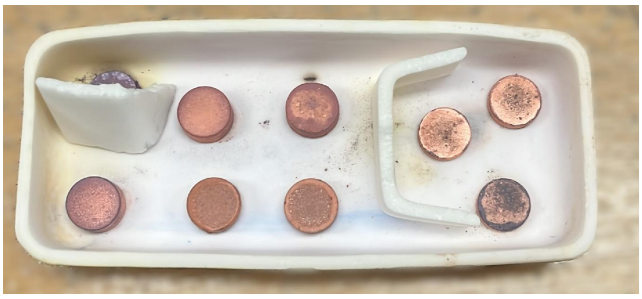

Figure 3.6: Hydraulic press setup used for cold pressing.

3.3 Microstructural Characterization

3.3.1 Scanning Electron Microscopy

Scanning electron microscopy (SEM) was used to evaluate the sample microstructure. More specifically, the distribution of the reinforcement phase in the copper matrix and the interface between the reinforcement phase and copper matrix. In addition, the changes in the microstructure after sintering and tribological testing were also investigated. SEM analysis was performed on selected pressed, sintered, polished, and tribologically tested samples.

3.3.1.1 Sample preparation

The sample preparation for SEM depended on the condition of the sample. Porous but compact samples, made from slurries with lower water content, required the longest preparation path, consisting of a sonication bath in ethanol, drying, gluing onto a SEM stub with carbon glue, and at least 1 h in a vacuum chamber before being placed on an appropriate holder in the SEM chamber. For composite powders, made from slurries with a higher water content, the powder was poured into aluminum foil placed in a Petri dish. The SEM stub was then glued with silver glue and dipped into the powder. Non-porous but compact samples, such as pressed or sintered samples, were taped to a SEM stub with conductive tape.

3.3.1.2 Instrument settings

The SE2 detector was primarily used, the imaging aperture was set to 1 and the accelerating voltage was set to 5 kV. Throughout the analysis the magnification

ranged from 500× to 3500×.

3.3.2 Energy-dispersive X-ray Spectroscopy

Energy-dispersive X-ray spectroscopy (EDS) was performed to identify the elements present on selected sample surfaces. EDS was also used to obtain elemental maps showing the spatial distribution of the detected elements in the selected area. The EDS analysis was performed together with SEM imaging, and no additional sample preparation was required.

In terms of instrument settings, the SE2 detector was used, the imaging aperture was set to 6, and the accelerating voltage was set to 25 kV. EDS was performed on areas captured at magnifications ranging from 100× to 1000×.

3.4 Tribological Testing

3.4.1 Linear Reciprocating Ball-on-Flat Measurements

Linear reciprocating tribological measurements were used to evaluate the CoF of the fabricated samples under sliding contact. The measurements were carried out using a CSM Instruments Linear Reciprocating Tribometer.

No additional sample preparation was required prior to testing in the linear reciprocating tribometer. However, selected samples were polished using PS 11 A silicon carbide abrasive paper with a grit size of 510 in order to investigate the effect of surface polishing on the frictional behaviour. The reciprocating sliding measurements were then repeated for these samples.

The counter body was a chrome steel ball with a diameter of 10 mm. All measurements were performed using a normal load of 3 N, a sliding speed of 5 cm/s and a total of 12500 cycles. Since all samples had a diameter of approximately 9 mm, the half amplitude was set to 4 mm for all measurements. The measurements ran in dry sliding conditions, meaning that no external lubricant was added. During

testing,the CoF was continuously recorded as a function of sliding cycles. If the CoF exceeded 2, the test was interrupted due to excessive friction.

3.4.2 Wear Track Analysis

Wear track analysis was performed after tribological testing to evaluate the surface damage caused by the reciprocating sliding contact. Optical microscopy was used as a fast and accessible method to obtain an overview of the wear track morphology and to quantify the wear track width.

After the tribological measurement, loose wear debris was gently removed from the wear track to facilitate transportation. The wear track region was analyzed at 5× magnification using the optical microscope to obtain an overview of the wear track morphology. The wear track width was quantified using the software measurement tool by measuring the width at approximately seven different positions. The mean wear track width was then calculated and used to compare the extent of surface damage between the different samples and sample groups.

4
Results

4.1 Overview of Investigated Samples

Table 4.1 gives an overview of the investigated sample groups included in this thesis. The samples groups consisted of pure copper references, MXene-Cu composites, Graphene-Cu composites, and MXene-Graphene-Cu hybrid composites. In addition to investigating the sintered samples, selected samples were investigated after surface polishing or in green body condition.

Sample group	**Investigated condition**	**Reinforcement loading**
Pure Cu reference	Sintered reference sample	–
Greased reference	Externally lubricated reference sample	–
MXene-Cu composites	Sintered samples	0.5, 1, 2, and 2.5 wt.% MXene
MXene-Cu composites	Green body sample	1 wt.% MXene
MXene-Cu composites	Polished sintered samples	2 and 2.5 wt.% MXene
Graphene-Cu composites	Sintered samples	0.5, 1, and 2 wt.% graphene
Graphene-Cu composites	Polished sintered sample	1 wt.% graphene
MXene-Graphene-Cu composites	Sintered samples	0.25 wt.% MXene + 0.25 wt.% graphene;

		0.5 wt.% MXene + 0.5 wt.% graphene; 1 wt.% MXene + 1 wt.% graphene
MXene-Graphene-Cu composites	Polished sintered samples	0.25 wt.% MXene + 0.25 wt.% graphene; 1 wt.% MXene + 1 wt.% graphene
MXene-Graphene-Cu composites	Green body samples	0.5 wt.% MXene + 0.5 wt.% graphene; 1 wt.% MXene + 1 wt.% graphene

Table 4.1: Overview of the investigated samples.

4.2 Microstructural Analysis

4.2.1 Reference Samples

Figure 4.1 shows SEM images of two reference MXene-Cu composite samples prepared with different mixing conditions.

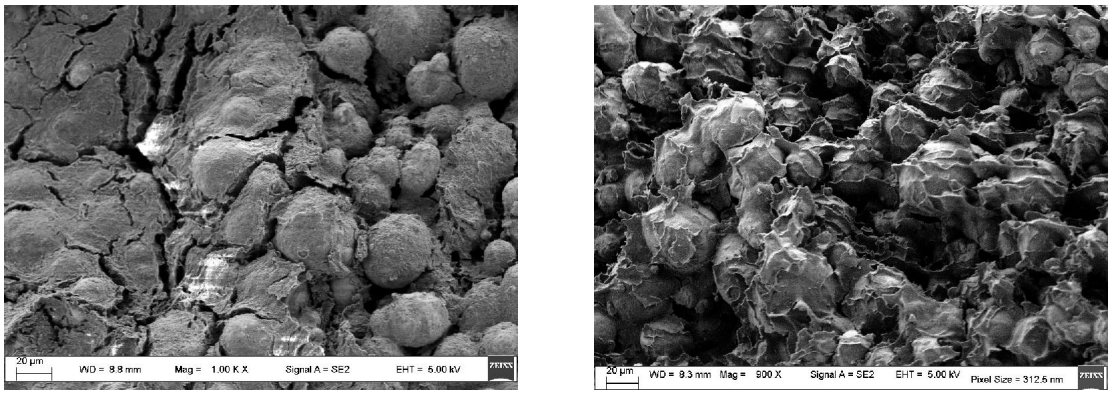

(a) Poorly mixed MXene-Cu composite mixture.

(b) Well-mixed MXene-Cu composite mixture.

Figure 4.1: SEM images of reference MXene-Cu composite samples prepared with different mixing conditions.

In the poorly mixed sample, the secondary phase appears unevenly distributed where some copper particles are completely encapsulated while. In contrast, the well-mixed sample shows a more continuous distribution of the secondary phase around the copper particles. Besides the difference in spatial distribution, the apparent thickness of the secondary phase also differs between the two samples.

4.2.2 Overview of Representative Pressed Sample Microstructures

Figure 4.2 shows SEM images of selected green body samples before sintering. The included samples are a pure copper reference, 0.5 wt.% MXene-Cu, and 1 wt.% MXene-Cu.

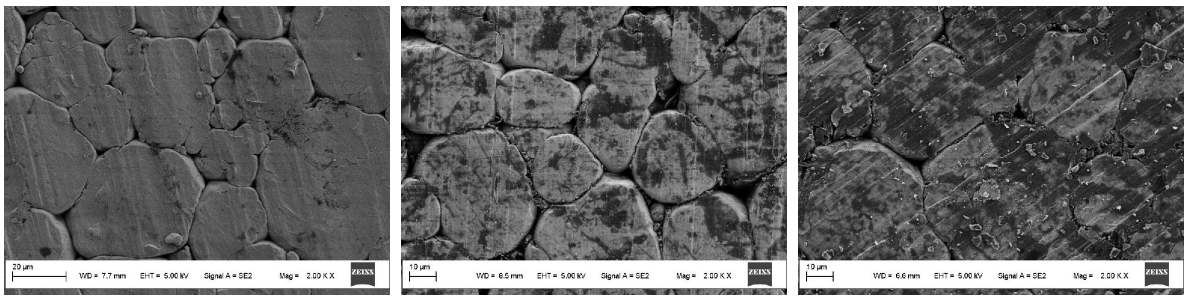

(a) Green body pure copper reference.

(b) Green body 0.5 wt.% MXene-Cu composite.

(c) Green body 1 wt.% MXene-Cu composite.

Figure 4.2: Representative SEM images of selected pressed samples before sintering.

Darker regions are visible on and around the lighter copper particles in the MXene-Cu composites. The amount of visible darker regions appears to increase with MXene loading. Copper-to-copper contact is present in all images.

4.2.3 Microstructure of Sintered MXene-Cu Composites

Figure 4.3 shows SEM images of the sintered MXene-Cu composites. The included MXene loadings are 0.5 wt.

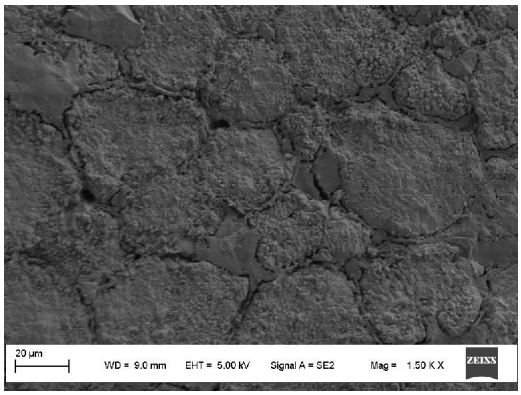

(a) Sintered 0.5 wt.% MXene-Cu composite.

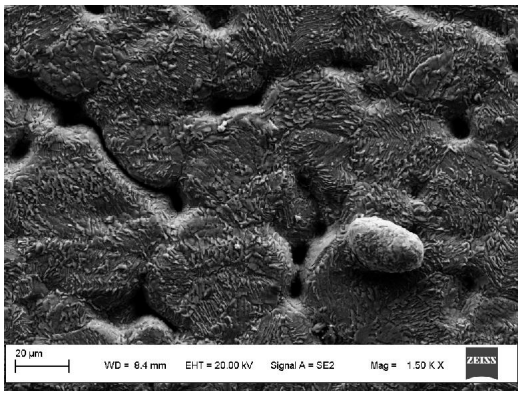

(b) Sintered 1 wt.% MXene-Cu composite.

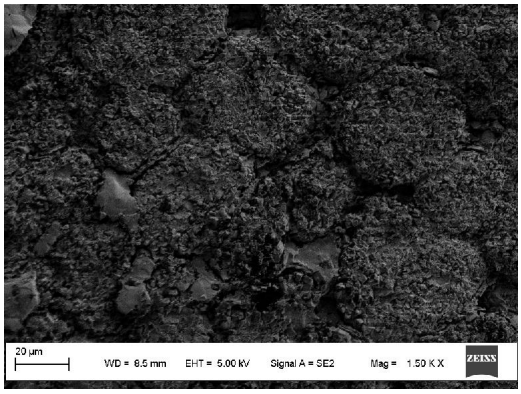

(c) Sintered 2 wt.% MXene-Cu composite.

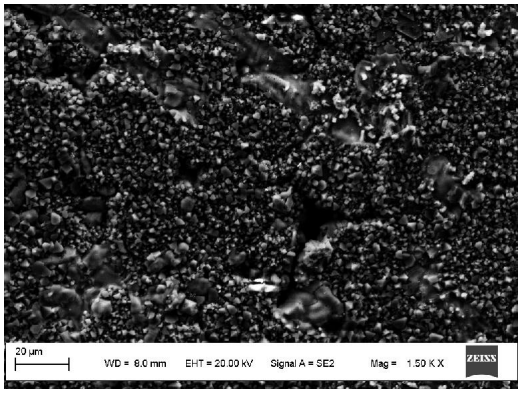

(d) Sintered 2.5 wt.% MXene-Cu composite.

Figure 4.3: SEM images of sintered MXene-Cu composites with different MXene loadings.

The grain-like structure observed in the green bodies remains after sintering. Larger grains appear to be surrounded by a secondary phase. As the MXene loading increases, the sprinkle-like surface texture becomes more prominent.

4.3 Wear Track Analysis

The wear track was analyzed qualitatively through investigating the morphology, using optical microscopy and SEM, and quantitatively through measuring the wear track width.

4.3.1 Optical Microscopy of Wear Tracks

Figure 4.4 shows optical microscopy images of the wear tracks after tribological testing for the MXene-Cu composites. The included MXene loadings are 0.5 wt.

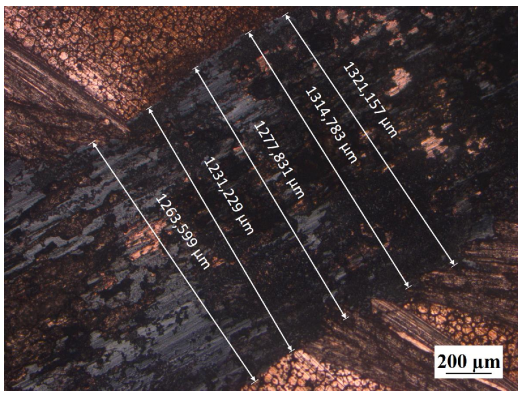

(a) 0.5 wt.% MXene-Cu wear track.

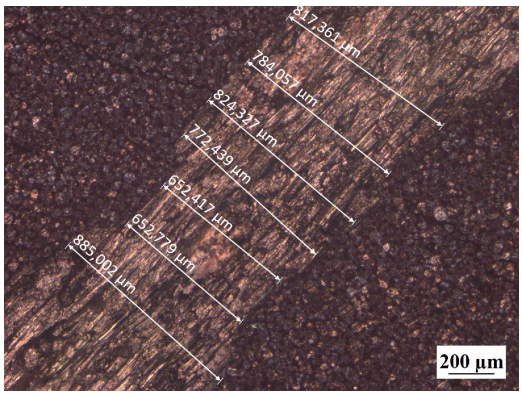

(b) 1 wt.% MXene-Cu wear track.

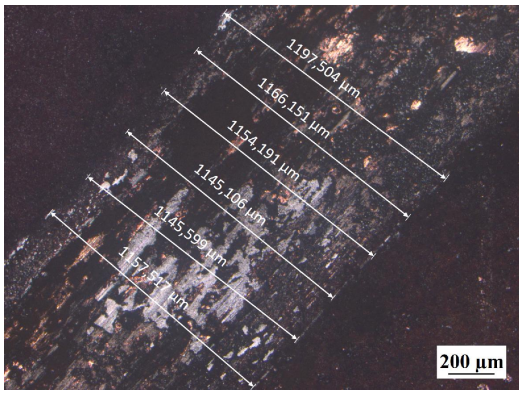

(c) 2 wt.% MXene-Cu wear track.

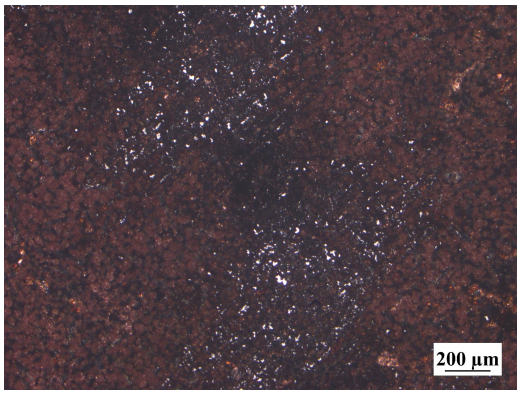

(d) 2.5 wt.% MXene-Cu wear track.

Figure 4.4: Optical microscopy images of wear tracks after tribological testing on MXene-Cu composites.

The MXene-Cu composites with MXene loadings of 0.5 wt.%, 1 wt.%, and 2 wt.% exhibit well-defined wear tracks after tribological testing, as shown in Figures 4.4a, 4.4b, and 4.4c. Among these composites, the 1 wt.% MXene-Cu composite exhibits the narrowest wear track, with a width ranging from 652 µm to 885 µm. In contrast, the 0.5 wt.% MXene-Cu composite exhibits the widest wear track, ranging from 1231 µm to 1321 µm. The tribological measurement of the composite with the highest MXene loading, 2.5 wt.%, did not yield a clearly defined wear track, making reliable width measurements difficult.

Figure 4.5 shows optical microscopy images of the wear tracks after tribological measurements for Graphene-Cu composites. included graphene loadings are 0.5 wt.%, 1 wt.%, and 2 wt.%.

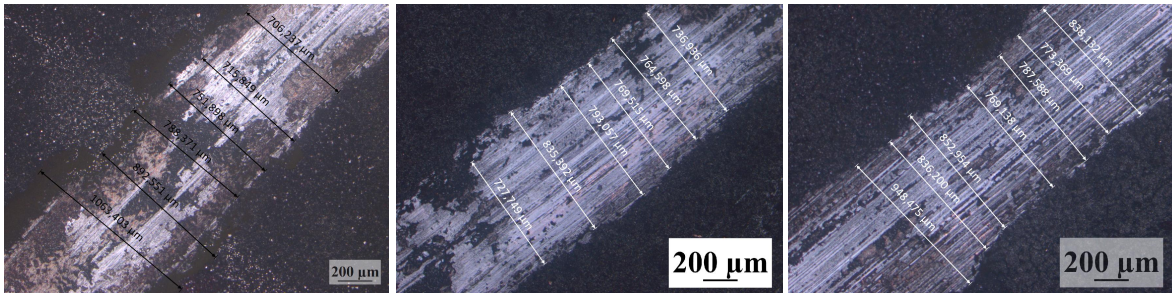

(a) 0.5 wt.% Graphene-Cu Wear Track

(b) 1 wt.% Graphene-Cu Wear Track

(c) 2 wt.% Graphene-Cu Wear Track

Figure 4.5: Optical Microscopy images of wear tracks after tribological measurements on Graphene-Cu composites.

The Graphene-Cu composite with graphene loadings of 1 wt.% and 2 wt.% exhibited well-defined wear tracks after tribological measurements (see Figures 4.5b and 4.5c).Amon these samples, the composite with the highest reinforcement loading, 2 wt.% graphene, exhibited the widest wear track, with a width ranging from 773 µm to 948 µm. In contrast, the composite with the lowest reinforcement loading, 0.5 wt.% graphene, did not exhibit a well-defined wear track (see Figure **??**). Instead, the wear track appeared patchy and contained regions with silvery-gray, dark and golden coloration. All graphene-Cu samples exhibited wear tracks with at least some silvery-gray regions.

4.3.2 Wear Track Width Quantification

The wear track widths measured from the optical microscopy images were averaged and summarized in Table 4.3 and Table 4.4. Figure 4.4 shows representative examples of how the wear track width was measured for the MXene-Cu samples. Additional examples of wear track width measurements for the remaining samples are provided in Appendix B.

Sample	Condition	Completed test	Wear track width [μm]
0.5 wt.% MXene-Cu	Unpolished	No	1282
1 wt.% MXene-Cu	Unpolished	Yes	770
2 wt.% MXene-Cu	Unpolished	Yes	1161
2 wt.% MXene-Cu	Polished	Yes	1736
2.5 wt.% MXene-Cu	Unpolished	Yes	-
2.5 wt.% MXene-Cu	Polished	Yes	1555
0.25 wt.% MXene-Graphene-Cu	Unpolished	Yes	854
0.25 wt.% MXene-Graphene-Cu	Polished	Yes	1265
0.5 wt.% MXene-Graphene-Cu	Unpolished	Yes	1624
1 wt.% MXene-Graphene-Cu	Unpolished	Yes	966
1 wt.% MXene-Graphene-Cu	Polished	Yes	1739
0.5 wt.% Graphene-Cu	Unpolished	Yes	820
1 wt.% Graphene-Cu	Unpolished	Yes	771
1 wt.% Graphene-Cu	Polished	Yes	1108
2 wt.% Graphene-Cu	Unpolished	Yes	829

Table 4.2: Mean wear track width measured from optical microscopy images.

4.3.3 SEM Analysis of Wear Track Morphology

Figure 4.6 shows SEM images of the wear tracks after the tribomechanical measurement has been performed. Included samples are 0.5 wt.% MXene-Cu, 1 wt.% MXene-Cu, 2 wt.% MXene-Cu, polished 2 wt.% MXene-Cu, 2.5 wt.% MXene-Cu, and polished 2.5 wt.% MXene-Cu.

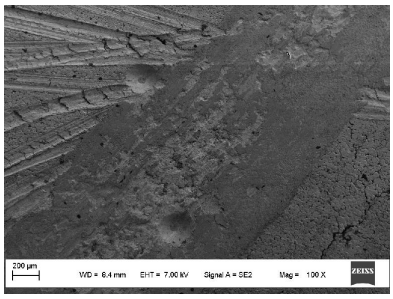

(a) 0.5 wt.% MXene-Cu wear track at 100× magnification.

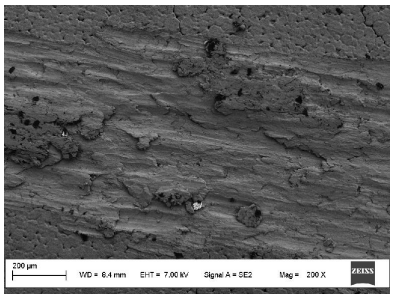

(b) 1 wt.% MXene-Cu wear track at 200× magnification.

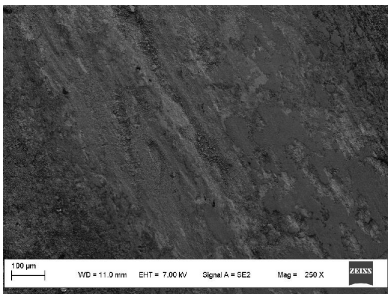

(c) 2 wt.% MXene-Cu wear track at 250× magnification.

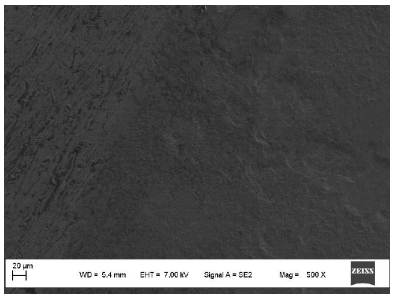

(d) Polished 2 wt.% MXene-Cu wear track at 500× magnification.

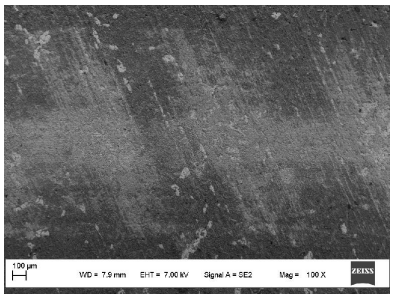

(e) 2.5 wt.% MXene-Cu wear track at 100× magnification.

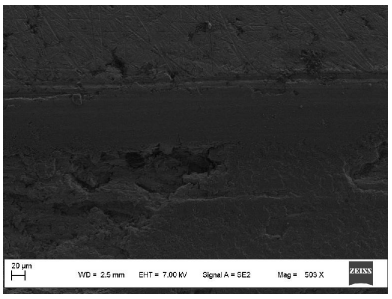

(f) Polished 2.5 wt.% MXene-Cu wear track at 500× magnification.

Figure 4.6: SEM images of selected MXene-Cu wear tracks after tribological testing.

Across the investigated samples, the wear tracks exhibit clear surface modification relative to the original microstructure. The type of surface modification differs between the samples. For example, the 1 wt.% MXene-Cu sample, shown in Figure 4.6b, and the 2 wt.% MXene-Cu sample, shown in Figure 4.6c, shows features consistent with surface smearing and redistributed material within the wear track. The polished samples also show visible wear tracks after testing, although the surface appearance differs from the corresponding unpolished samples. The wear track regions of the polished 2 wt.% MXene-Cu sample and the polished 2.5 wt.% MXene-Cu sample appears flatter and shows possible delamination-like features.

Figure 4.7 shows SEM images of the wear tracks after the tribomechanical measurement has been performed. Included samples are 0.5 wt.% Graphene-Cu, 1 wt.% Graphene-Cu and 2 wt.% MXene-Cu.

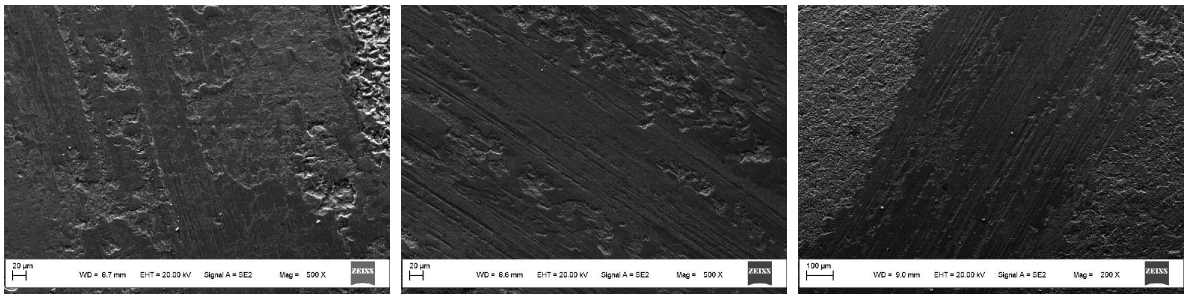

(a) 0.5 wt.% Graphene-Cu wear track at 500× magnification.

(b) 1 wt.% Graphene-Cu wear track at 500× magnification.

(c) 2 wt.% Graphene-Cu wear track at 200× magnification.

Figure 4.7: SEM images of selected Graphene-Cu wear tracks after tribological testing.

Across the investigated samples, the wear tracks exhibit clear surface modification relative to the original microstructure. However, all wear tracks from Graphene-Cu composites show flatter features consistent with parallel grooves and possible delamination-like features.

The morphology of the wear track for the Graphene-Cu composite differs from that of the MXene-Cu composites. While the unpolished MXene shows in general features that are more consistent with surface smearing and redistributed material within the wear track, the Graphene-Cu sample shows features that are more consistent with parallel grooves and delamination-like features.

4.4 EDS analysis

The general microstructure and wear tracks of selected samples were further examined using energy-dispersive X-ray spectroscopy (EDS). The analysis focused on the elemental distribution of copper (Cu), titanium (Ti), oxygen (O), aluminum (Al), carbon (C), and fluorine (F). Copper was used to identify the metal matrix, while titanium served as the primary indicator of MXene-related regions. The remaining elements were qualitatively evaluated to assess local variations in surface composition.

4.4.1 General microstructure and effect of polishing

Figure 4.8 shows the EDS elemental maps obtained from the selected area of the 2.5 wt.% MXene-Cu sample.

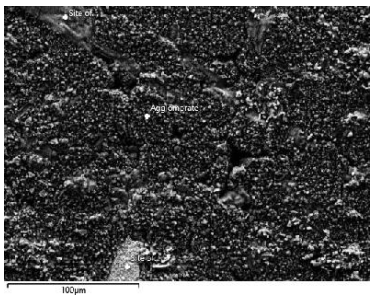

(a) Corresponding electron image of the selected EDS analysis area.

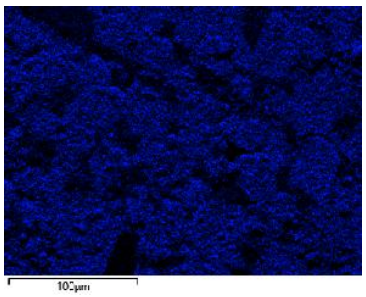

(b) O elemental map.

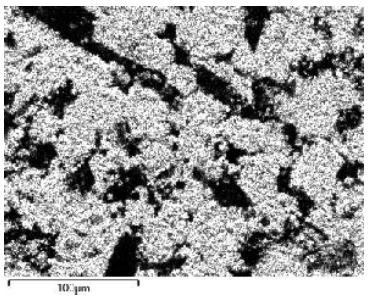

(c) Al elemental map.

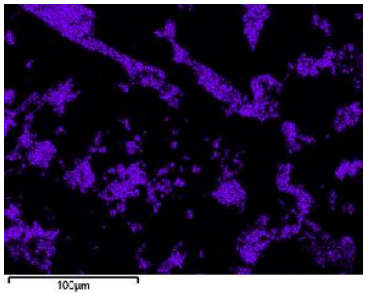

(d) Ti elemental map.

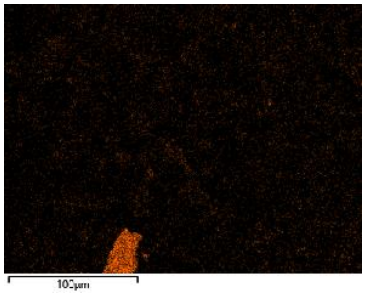

(e) Cu elemental map.

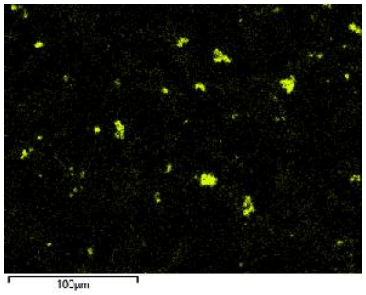

(f) F elemental map.

Figure 4.8: EDS elemental maps of the selected area on the 2.5 wt.% MXene-Cu composite.

The detected elements in the selected area were O, Al, Ti, Cu, and F. The elemental maps show that the selected area is mainly characterized by O-, Al-, and Ti-rich regions, while the Cu and F signals are more localized. The O and Al signals appear to overlap spatially, whereas the Ti signal is mainly located between these O- and Al-rich regions. Smaller F-rich regions are also observed between the O- and Al-rich regions. In addition, one larger Cu-rich region is present in the selected area.

Figure 4.9 shows the EDS elemental maps obtained from the selected area of the polished 2.5 wt.% MXene-Cu sample.

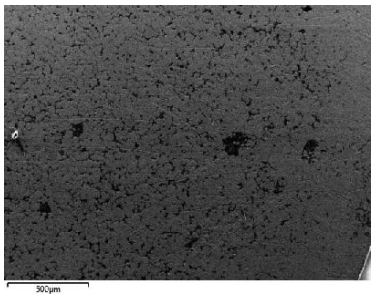

(a) Corresponding electron image of the selected EDS analysis area.

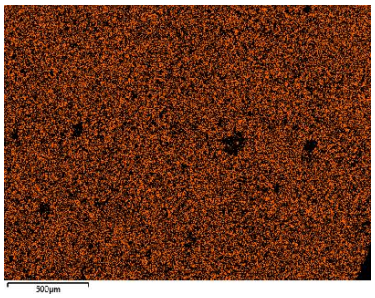

(b) Cu elemental map.

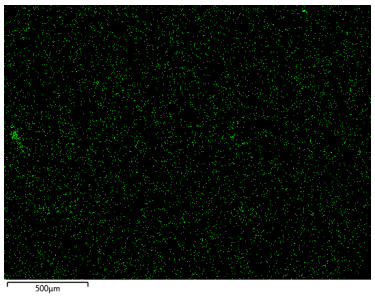

(c) C elemental map.

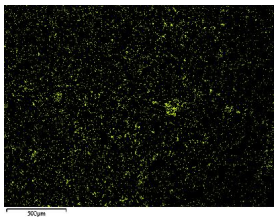

(d) F elemental map.

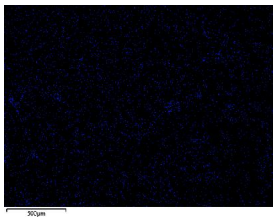

(e) O elemental map.

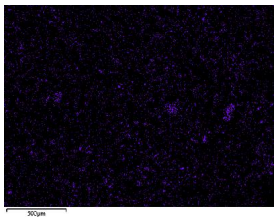

(f) Ti elemental map.

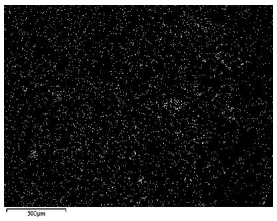

(g) Al elemental map.

Figure 4.9: EDS elemental maps of the selected area on the polished 2.5 wt.% MXene-Cu composite.

The elements detected in the selected area of the polished sample were Cu, C, F, O, Ti, and Al. The selected area was dominated by the Cu signal, while smaller localized regions containing C, F, O, Ti, and Al were observed.

The EDS analysis of the polished surface, shown in Figure 4.9, differs from the unpolished surface shown in Figure 4.8. For the polished sample, the visible Al-, O-, and Ti-rich regions decreased, while the selected surface region became dominated by Cu.

Figure 4.10 shows the EDS elemental maps obtained from the selected area of the 0.5 wt.% Graphene-Cu sample.

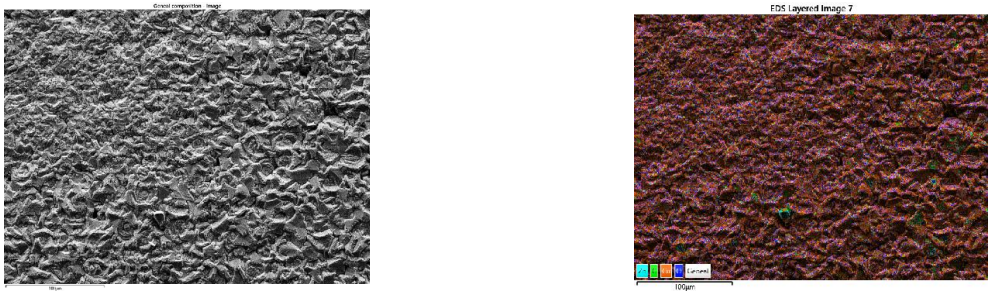

Figure 4.10: EDS data of general composition of 0.5 wt.% Graphene-Cu composite.

The EDS data for the general composition of the 0.5 wt.% Graphene-Cu composite shows that the present elements on the sample surface are Cu, C, O, and Zn. The sample surface mainly consists of Cu, but also C and O.

4.4.2 Wear track composition

Figure 4.11 shows EDS elemental maps obtained from the selected wear track area on the 1 wt.% MXene-Cu green body.

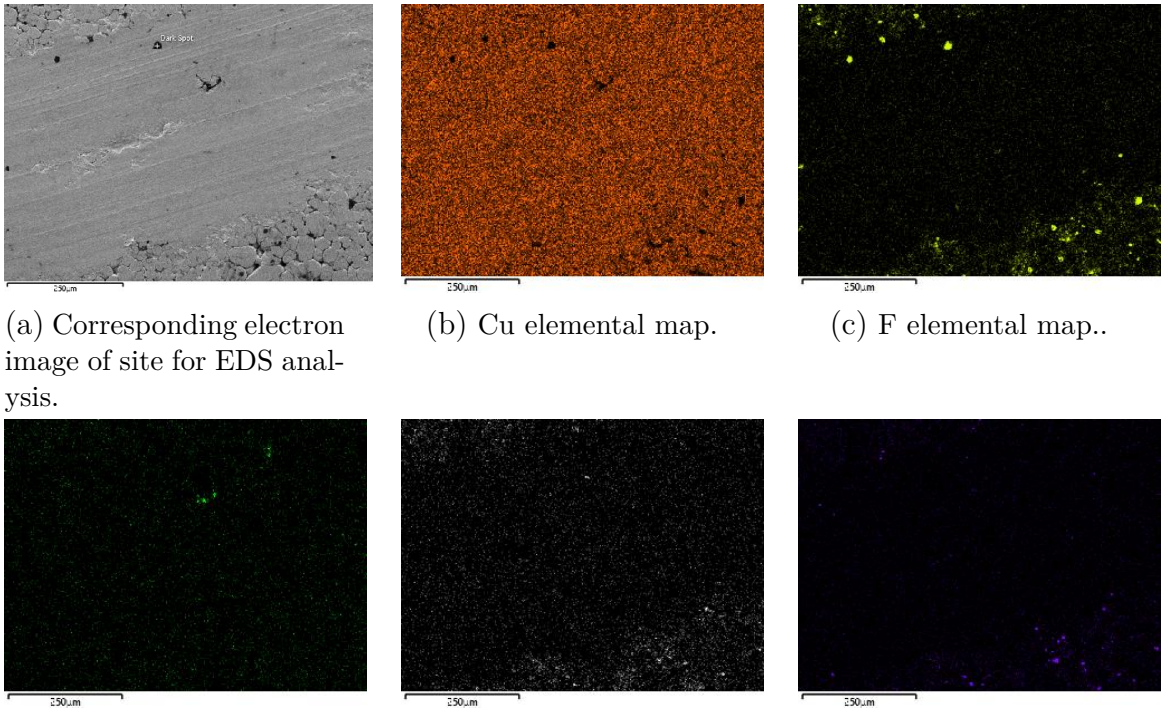

(a) Corresponding electron image of site for EDS analysis.

(b) Cu elemental map.

(c) F elemental map..

(d) C elemental map.

(e) Al elemental map.

(f) Ti elemental map.

Figure 4.11: EDS elemental maps of the selected area of the wear track on 1 wt.% MXene-Cu greenbody.

The elements detected in the selected area of the green body 1 wt.% MXene-Cu

sample were Cu, F, C, Al, and Ti. The selected area was dominated by a relatively homogeneous Cu signal. While F, Al and Ti signals were mainly observed outside the wear track region, the wear track was primarily Cu-rich with smaller localized C-rich regions.

Figure 4.12 shows EDS elemental maps onbtained from the selected wear track area on the 2 wt.% MXene-Cu sample.

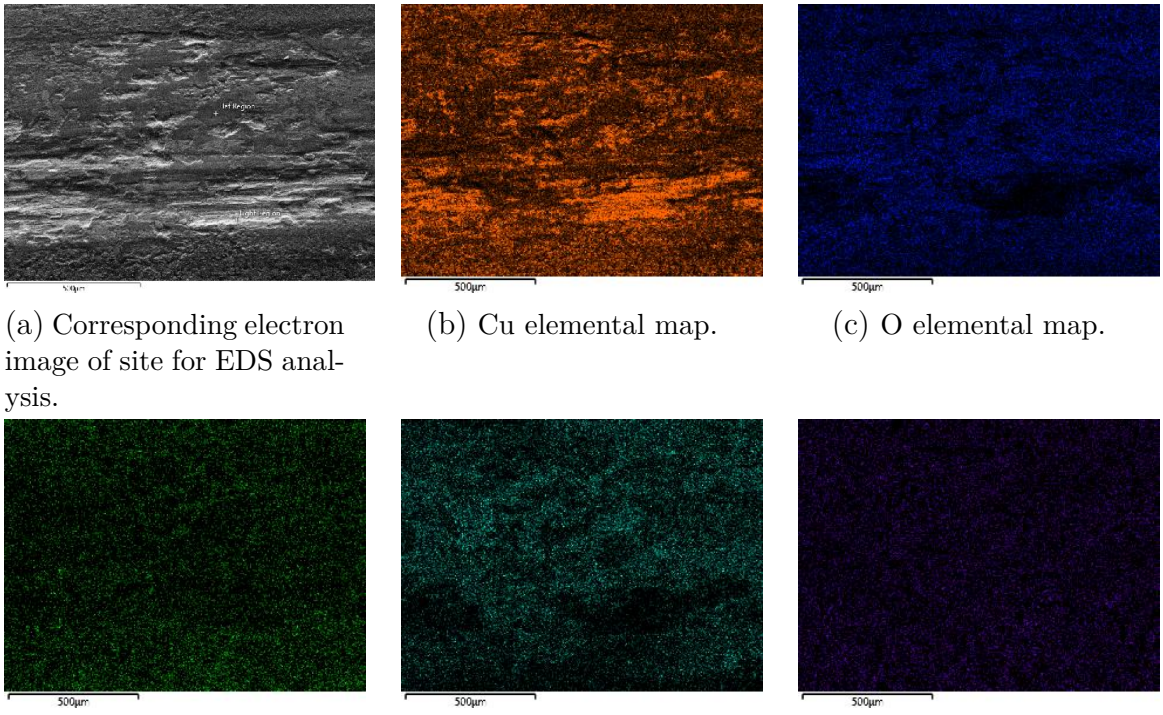

(a) Corresponding electron image of site for EDS analysis.

(b) Cu elemental map.

(c) O elemental map.

(d) C elemental map.

(e) Fe elemental map.

(f) Ti elemental map.

Figure 4.12: EDS elemental maps of the selected area of the wear track on 2 wt.% MXene-Cu.

The elements detected in the selected ares on the 2 wt.% MXene-Cu wear track were Cu, O, C, Fe, and Ti. The selected area was mainly characterized by Cu and O signals. The light and compacted region annotated as "Light Region" in Figure 4.12a was dominated by Cu-rich signals and showed lower O and Fe signals compared with the surrounding wear track area.

Figure 4.13 shows EDS elemental maps obtained from the selected wear track area

on the polished 2 wt.% MXene-Cu sample.

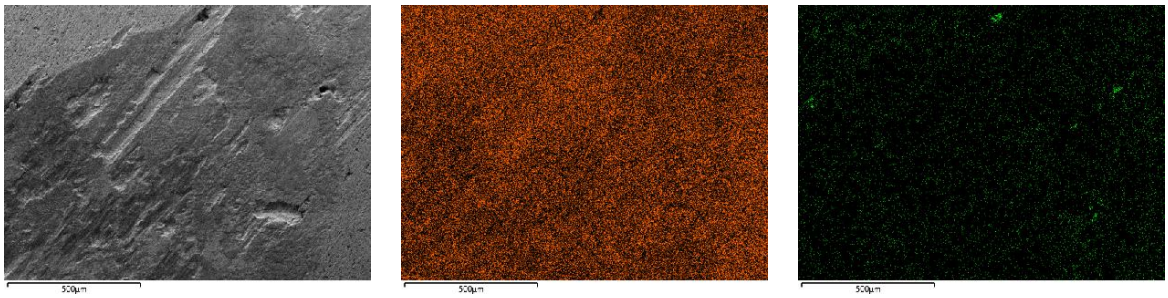

(a) Corresponding electron image of site for EDS analysis.

(b) Cu elemental map.

(c) C elemental map.

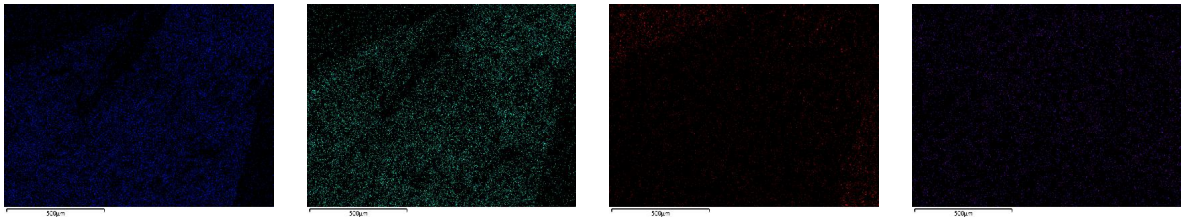

(d) O elemental map.

(e) Fe elemental map.

(f) Si elemental map..

(g) Ti elemental map.

Figure 4.13: EDS elemental maps of the selected area of the wear track on polished 2 wt.% MXene-Cu.

The elements detected on the selected area of the polished 2 wt.% MXene-Cu wear track were Cu, C, O, Fe, Si and Ti. The selected area was dominated by Cu-signals.

Figure 4.14 shows EDS elemental maps obtained from the selected wear track area on the 2.5 wt.% MXene-Cu sample.

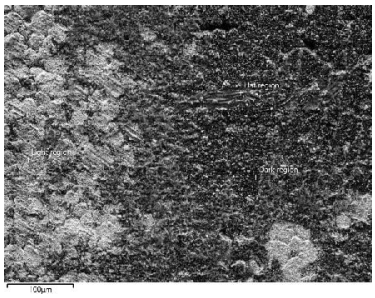

(a) Corresponding electron image of site for EDS analysis.

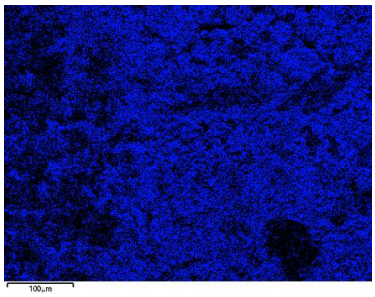

(b) O elemental map.

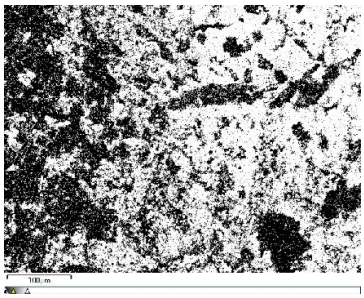

(c) Al elemental map.

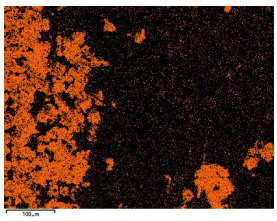

(d) Cu elemental map.

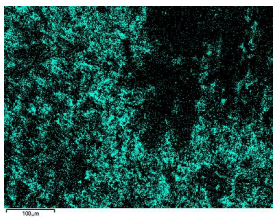

(e) Fe elemental map.

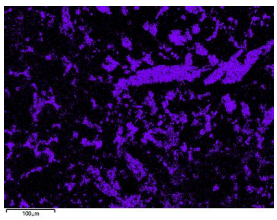

(f) Ti elemental map.

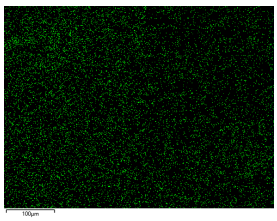

(g) C elemental map.

Figure 4.14: EDS elemental maps of the selected area of the wear track on 2.5 wt.% MXene-Cu.

The elements detected on the selected area of the 2.5 wt.% MXene-Cu wear track were O, Al, Cu, Fe, Ti and C. The lighter region outside the wear track was mainly characterized by the Cu signal, while the darker and flatter wear track region was mainly characterized by O, Al, and Ti signals.

Figure 4.15 shows EDS elemental maps obtained from the selected wear track area on the polished 2.5 wt.% MXene-Cu sample.

(a) Corresponding electron image of site for EDS analysis at wear track.

(b) Copper.

(c) Carbon.

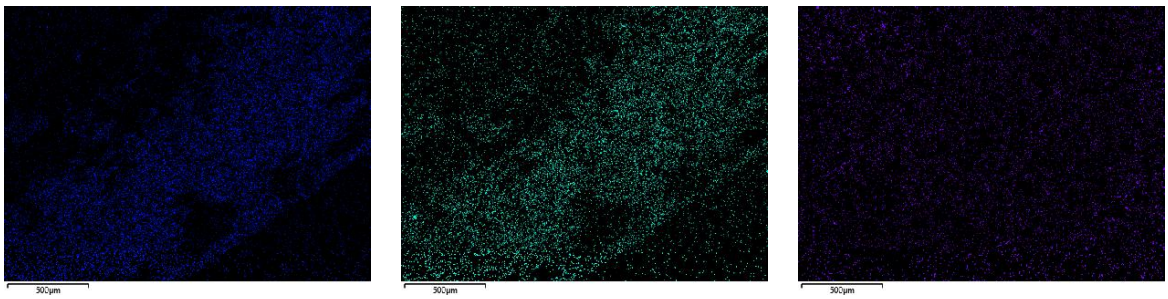

(d) Oxygen.

(e) Iron.

(f) Titanium.

Figure 4.15: EDS elemental maps of the wear track on polished 2.5 wt.% MXene-Cu.

The elements detected on the selected area of the polished 2.5 wt.% MXene-Cu wear track were O, Al, Cu, Fe, Ti and C. The wear track region was mainly characterized by O and Ti signals, while the surrounding composite surface was mainly characterized by Cu and Fe signals. In contrast to the other detected elements in this selected area, the C signal appeared more evenly distributed across the selected area.

4.5 Tribomechanical Measurements

4.5.1 Friction Behavior of MXene-Cu Composites

Figure 4.16 shows how the CoF evolves during sliding cycles for the MXene-Cu composites. A greased reference, a copper reference and MXene-Cu composites with MXene loadings of 0.5 wt.%, 1 wt.%, 2 wt.% and 2.5 wt.% MXene are included in the figure.

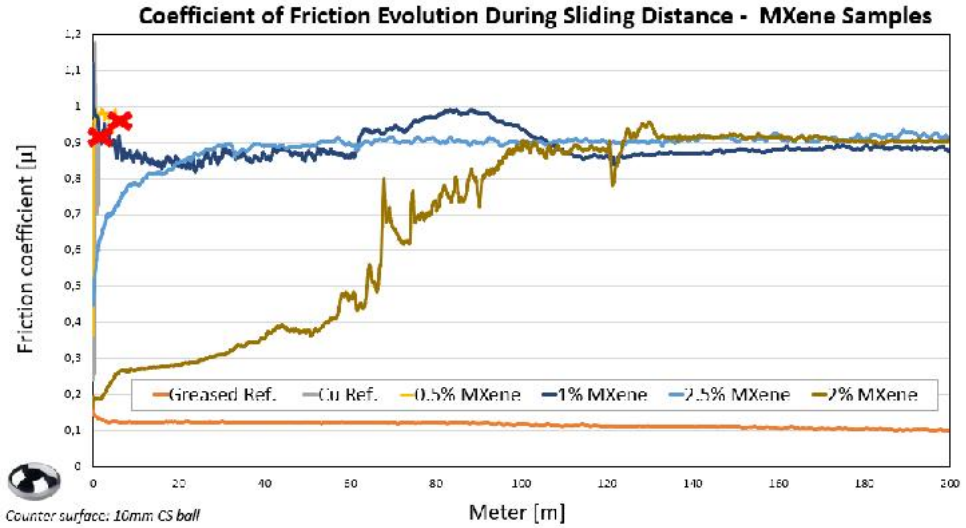

Figure 4.16: Coefficient of friction as a function of sliding distance for the MXene-Cu composites, pure copper reference, and greased reference.

Overall, the measured samples showed a relatively high CoF and none achieved a CoF comparable to the greased reference. However, differences were observed between the samples regarding the stability and whether they completed the full measurements. Both the pure Cu reference and the 0.5 wt.% MXene-Cu composite were interrupted at an early stage in the measurements due to excessive friction, as indicated by two red crosses in the graph. The 1 wt.% and 2.5 wt.% MXene-Cu composite showed high but relatively stable CoF throughout the measurements. In contrast, the 2 wt.% MXene-Cu composite exhibited a lower CoF for the first approximately 60 m before finalizing the measurement at a similar CoF to previously mentioned composites.

4.5.2 Effect of Surface Polishing on MXene-Cu Composites

To investigate the influence of the surface condition on the frictional behavior, Figure 4.17a compares the CoF evolution of MXene-Cu composite samples before and after surface polishing. Prior to the tribological testing, the samples were polished using abrasive paper, as described in Section 3.4.1. Figure 4.17b shows a magnified view of the initial 50 m of sliding from Figure 4.17a to get a more detailed picture of the early stages of measurement.

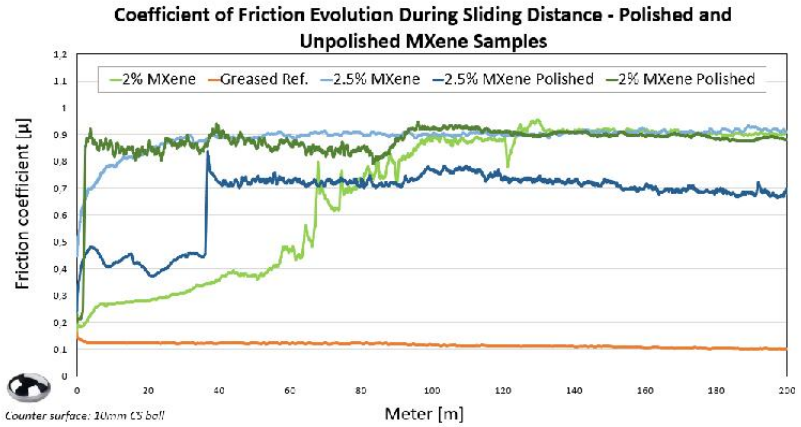

(a) Coefficient of friction as a function of sliding distance for the polished and unpolished MXene-Cu composites and greased reference.

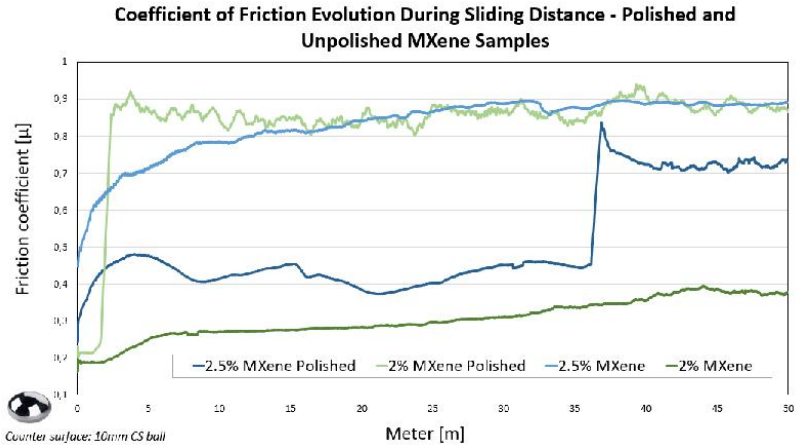

(b) Coefficient of friction as a function of sliding distance for the polished and unpolished MXene-Cu composites. First 50 m.

Figure 4.17: Coefficient of friction as a function of sliding distance for selected MXene-Cu composites.

The two MXene-Cu composites, with MXene loadings of 2 wt.% and 2.5 wt.% respectively, respond differently to polishing the sample surface prior to testing. After being polished, the CoF of the 2.5 wt.% MXene-Cu composite decreased at early stage of measurement. The polished 2.5 wt.% MXene-Cu composite maintains a relatively low CoF for approximately 40 m before rising sharply and stabilizing again at a higher CoF. The CoF of the 2 wt.% MXene-Cu composite, on the other hand, increases significantly when polished. While the unpolished 2 wt.% MXene-Cu composite maintains a relatively low CoF for over 60 m the polished sample demonstrates a sharp increase shortly after the start of the measurement.

4.5.3 Effect of Sintering on the Friction Behavior of MXene-Cu Composites

To investigate the influence of the processing, Figure 4.18 compares the CoF evolution of sintered and green body MXene-Cu composites.

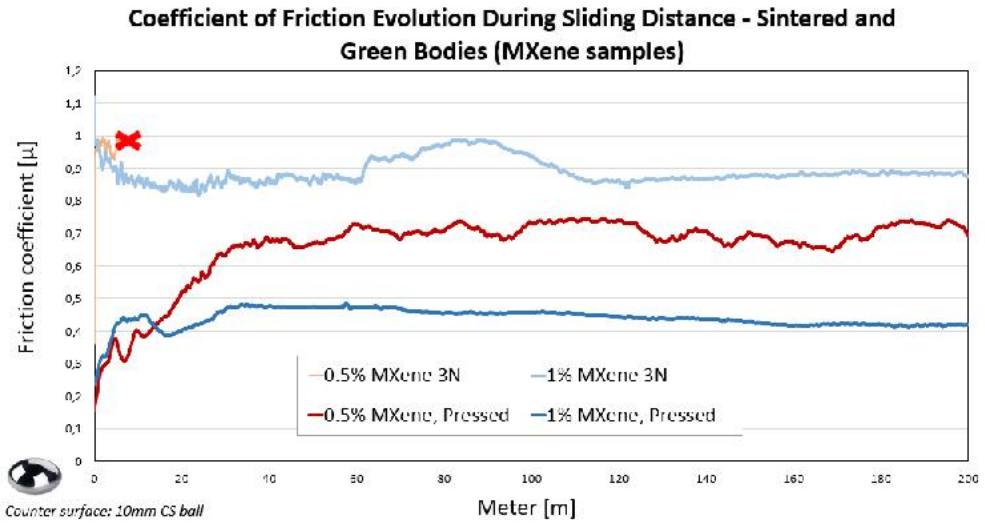

Figure 4.18: Coefficient of friction as a function of sliding distance for green body and sintered MXene-Cu composites.

Both green body MXene-Cu composites completed the full tribological measurement and showed lower CoF values than their corresponding sintered samples. While the sintered 0.5 wt.% MXene sample was interrupted at an early stage of the measurement due to excessive friction, the corresponding green body sample finished the measurement. Furthermore, the green body 1 wt.% MXene sample exhibited an overall lower CoF than the corresponding sintered sample.

4.5.4 Friction Behavior of Graphene-Containing Cu Composites

Figure 4.19a shows how the CoF evolves over sliding cycles for MXene-Graphene-Cu composites. A greased reference, a copper reference and MXene-Graphene-Cu composites with MXene and Graphene loading of 0.25 wt.%, 0.5 wt.% and 1 wt.% respectively are included in the figure. Figure 4.19b shows how the CoF evolves over sliding cycles for Graphene-Cu composites. A greased reference, a copper reference and Graphene-Cu composites with graphene loading of 0.5 wt.%, 1 wt.% and 2 wt.%

are included in the figure.

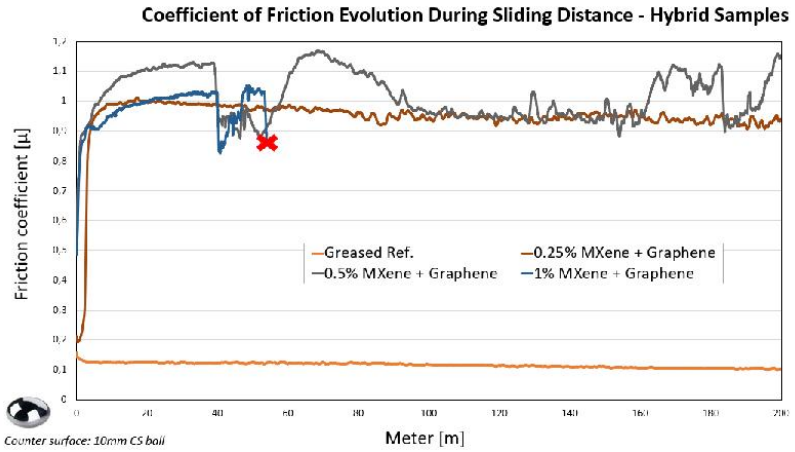

(a) Coefficient of friction as a function of sliding distance for MXene-Graphene-Cu samples and a greased reference.

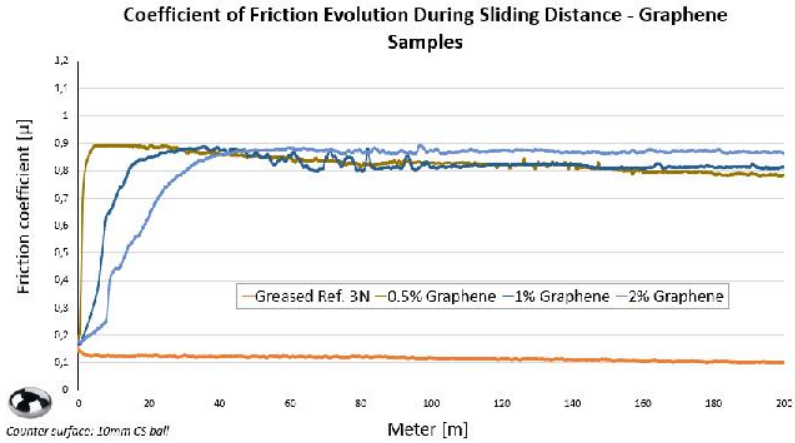

(b) Coefficient of friction as a function of sliding distance for Graphene-Cu samples and a greased reference.

Figure 4.19: Coefficient of friction as a function of sliding distance for graphene-containing composites.

Overall, none of the MXene-Graphene-Cu composites or the Graphene-Cu composites achieved a CoF comparable to the greased reference. Differences were observed between the samples, mainly regarding the stability but also wether they completed the full measurements. The 1 wt.% MXene + Graphene composite was interrupted at an early stage in the measurements due to excessive friction, as indicated by the red cross in Figure 4.19a. The 0.5 wt.% MXene + 0.5 wt.% graphene composite completed the measurement, but the measured CoF fluctuated between approximately 0.9 and 1.2. The relatively large fluctuation in CoF indicates a more unstable sliding

behavior compared to the other graphene-containing composites that completed the full measurement included in Figure 4.19a and Figure 4.19b.

4.5.5 Effect of Surface Polishing on graphene-containing composites

To investigate the influence of the surface condition on the frictional behavior, Figure 4.20a compares the CoF evolution of MXene-Graphene-Cu composite samples before and after surface polishing. Prior to the tribological testing, the samples were polished using abrasive paper, as described in Section 3.4.1. Figure 4.20b shows a magnified view of the initial 50 m of sliding from Figure 4.20a to get a more detailed picture of the early stages of measurement.

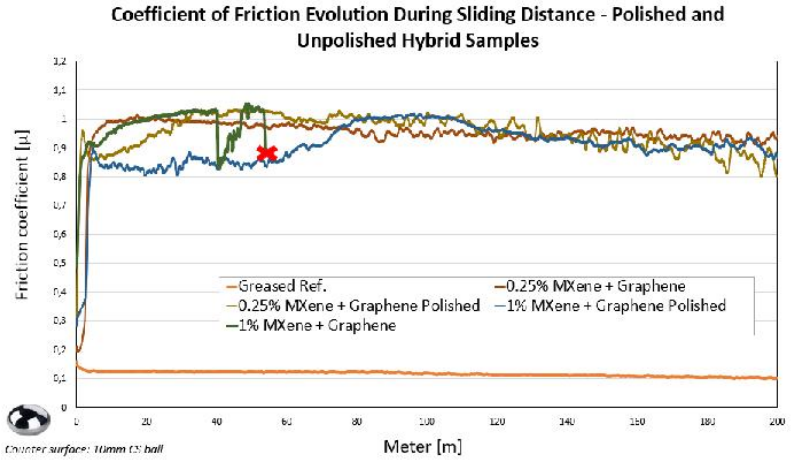

(a) Coefficient of friction as a function of sliding distance for the polished and unpolished MXene-Graphene-Cu composites and greased reference.

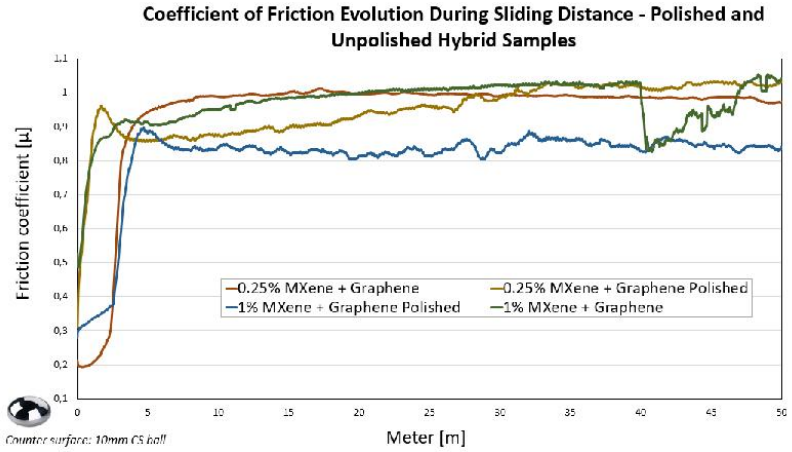

(b) Coefficient of friction as a function of sliding distance for the polished and unpolished MXene-Cu composites and greased reference. First 50 m.

Figure 4.20: Coefficient of friction as a function of sliding distance for polished and unpolished graphene-containing composites.

The two MXene-Graphene-Cu composites, with loadings of 1 wt.% MXene + 1 wt.% graphene and 0.25 wt.% MXene + 0.25 wt.% graphene, respectively, respond differently to polishing the sample surface prior to tribomechanical testing. Before being polished, the 1 wt.% MXene + 1 wt.% graphene sample was interrupted at an early stage in the measurement, annotated by a red cross in the graph. After polishing, the 1 wt.% MXene + 1 wt.% graphene sample finished the measurement and maintained an initially lower CoF compared to the other samples in Graph 4.20b. For the 0.25 wt.% MXene + 0.25 wt.% graphene sample, on the other hand, there was no significant change in the evolution of CoF, which can be observed.

4.5.6 Measurement Variability

Figure 4.21 shows the evolution of CoF during sliding distance for two separate measurements on the same sample, but at different spots.

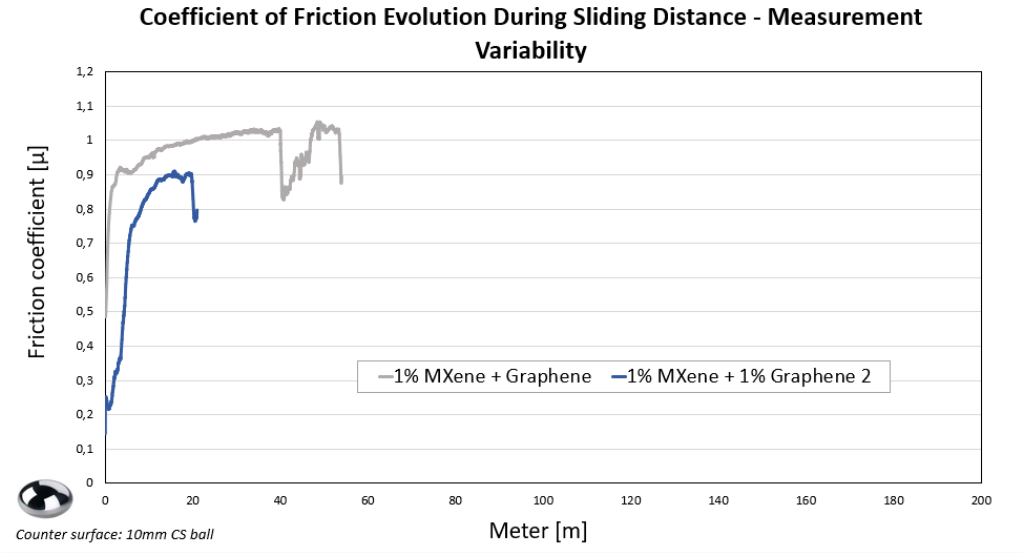

Figure 4.21: Measurement variability for 1 wt.%MXene + 1 wt.% Graphene tribological measurement.

The two measurements result in different evolution of CoF during sliding distance. The first measurement of the 1 wt.% MXene + 1 wt.% Graphene slid for longer before being interrupted due to excessive friction. Additionally, the measurement exhibited a generally higher CoF. The second measurement at the same sample, but at a fresh spot was interrupted earlier due to excessive friction but exhibited a generally lower CoF compared to first measurement.

4.5.7 Mean Coefficient of Friction

MXene content [wt.%]	Condition	Finished Measurement [Y/N]	Mean CoF
0.5	Sintered	N	0.949
0.5	Pressed	Y	0.661
1	Sintered	Y	0.877
1	Pressed	Y	0.411
2	Sintered	Y	0.62
2	Polished	Y	0,872
2.5	Sintered	Y	0.906
2.5	Polished	Y	0,788

Table 4.3: Mean coefficient of friction for all the investigated MXene-Cu composites.

MXene content [wt.%]	Graphene content [wt.%]	Condition	Finished Measurement [Y/N]	Mean CoF
0.25	0.25	Sintered	Y	0,869
0.25	0.25	Polished	Y	0,901
0.5	0.5	Sintered	Y	0,929
0.5	0.5	Pressed	N	0.256
1	1	Sintered	N	0,909
1	1	2nd measurement	N	0,745
1	1	Polished	Y	0,867
1	1	Pressed	Y	0.507
0	0.5	Sintered	Y	0,833
0	1	Sintered	Y	0,78
0	1	Polished	Y	0,857
0	2	Sintered	Y	0,774

Table 4.4: Mean coefficient of friction for all the investigated Graphene-containing Cu composites.

5
Discussion

5.1 Did MXene improve the tribological performance of Cu?

While the Cu reference was interrupted at an early stage in the measurement due to excessive friction, all the MXene reinforced samples lasted longer and all but one sample (the lowest loading sample) finished the measurement (Figure 4.16). This indicates an improvement in sliding durability when reinforcing the Cu matrix with MXene. However, the measured CoF remained relatively high, ranging from 0.62 to 0.949, for all MXene-Cu samples (Table 4.3).

The morphology captured by the SEM images of the wear tracks differs between the samples (Figure 4.6). However, all wear tracks show flattened regions, possibly from plastic deformation. The measured wear track width ranged from 770 µm to 1282 µm for the MXene-Cu samples (Table 4.2). Using the wear track width as an indication of wear damage complicates the possible conclusions from the CoF data, as it does not appear to be a relationship between wear track width and mean CoF. This makes the potential impact of reinforcing the sample on the tribological properties more complex and case dependent.

While the reinforcement improved the ability to sustain sliding contact, it failed at producing and maintaining a considerable reduction in friction. In addition, the visible wear damage that occurred after sliding, varied between the samples.

5.2 Influence of MXene loading

When comparing the MXene samples, the extent of the tribological improvement, both in terms of mean CoF and visible damage, appears to depend on the reinforcement loading (Fig 4.16).

Among the MXene samples, the 0.5 wt.% MXene sample achieved the highest mean CoF of 0.949 (Table 4.3). While the sample lasted longer in the tribological measurements than the pure Cu reference, the measurement was still interrupted at an early stage due to excessive friction. The observations from the wear track might stem from the ductility of Cu, which causes it to deform rather than fracture. The wear track contains large flattened and smooth regions (Figure 4.6a). That suggests that material has been plastically deformed and smeared across the surface during sliding. Since the matrix is Cu-based, this makes sense because Cu is ductile and can deform rather than fracture cleanly. In addition, the sample measured the broadest wear track width of 1282 µm (Table 4.2). This may indicate more wear damage compared to the other samples. The high CoF, interrupted measurement, and wear track morphology and width indicates poor tribological performance. One possible explanation to the poor performance is that 0.5 wt.% MXene was insufficient loading to benefit from the potential enhancement of tribological properties seen in theory when incorporating MXenes.

The 1 wt.% MXene sample exhibited a mean CoF of 0.877 (Table 4.3). The wear track has many smeared, flattened and elongated regions (Figure 4.6b). This suggests that the material has been plastically deformed and smeared across the surface during sliding. This might indicate that the dominant wear mechanisms were adhesive wear accompanied by plastic deformation and material smearing. As discussed previously, the ductility of Cu makes deformation more plausible than a clean fracture. The sample also measured the narrowest mean wear track of 770 µm (Table 4.2). This may indicate less wear damage compared to the other samples. While the sample underwent adhesive wear and plastic deformation during sliding the narrow

wear track width may indicate that the material resisted wear damage better than the other samples. When comparing to the 0.5 wt.% MXene samples, the increased sliding stability, lower CoF and narrow wear track indicates improved tribological performance.

One notable result is the MXene-Cu sample with 2 wt.% MXene as it maintained a CoF below 0.5 for the initial 60 m before increasing to approximately 0.9 (Figure 4.16) and finishing the measurement with a mean CoF of 0.62 (Table 4.3). The EDS analysis on the region shows the presence of Cu, O, C, Fe with small traces of Ti on the wear track (Figure 4.12). When evaluating the elemental mapping from the EDS analysis, there is a flat region with less Cu and more O and Fe. However, the already small amount of Ti, which is used to detect MXenes, is homogeneously distributed across the wear track area. Based on the EDS analysis, there is no indication that MXenes have accumulated at the contact area or contributed to the initial low CoF. Therefore, the smooth and flattened regions seen in SEM images (Figure 4.6c) are likely due to plastic deformation and material smearing. The sample also measured a relatively broad wear track width at 1161 µm (Table 4.2). This width may indicate a similar wear damage to the other samples. While this sample exhibits an initial improvement in friction, compared to the other MXene-Cu samples, the EDS analysis does not support a sustained lubrication mechanism driven by MXene. Instead the analysis states that the wear track area mainly consists of Cu.

The 2.5 wt.% MXene sample had the highest MXene loading of the included samples, and measured a relatively high mean CoF at 0.906 (Table 4.3). The sample is notable as the tribological measurement did not result in a well-defined wear track, but a zig-zag looking pattern (Figure 4.6e). The absence of a continuous wear track suggests that the higher MXene loading might have affected surface homogeneity and therefore caused an unstable wear-track formation. In addition, the irregular wear track made it difficult to estimate a reliable wear track width. The EDS analysis of the wear track shows the presence of O, Al, Cu, Fe, Ti and C (Figure 4.14). In addition, the elemental mapping shows a distinct difference between the

wear track region and the composite surface. While the wear track region is dominated by spatially separated Ti-rich and Al/O-rich regions, the composite surface is dominated by Cu. After the sliding, Ti-containing material was present at the contact area. However, the high CoF and irregular wear track indicate that the Ti-rich material present at the contact area did not produce stable lubrication. The sample with the highest MXene loading, showed the most Ti-rich regions, both in the general sample surface (Figure 4.8) but also at the wear track. However, considering the poor tribological performance in terms of CoF and wear track morphology, more exposed Ti does not appear to automatically improve tribological performance.

These results indicate that a higher MXene loading does not generate better results. Instead, an intermediate MXene loading indicates more favorable results. This might be due to processability issues.While a sufficient MXene loading is required to achieve sliding stability, and some enhanced tribological properties such as a lower mean CoF and a more narrow wear track, too much MXene might lead to the formation of agglomerates and hinder sintering.

5.3 Relationship between microstructure and tribological performance

The processing route had a clear influence on the observed microstructure of the MXene-Cu composites. As shown by the reference samples in Figure 4.1, freeze-drying alone did not create a homogeneous dispersion. Instead, the comparison indicates that the quality of the slurry mixing step was critical, while rapid freezing and subsequent freeze-drying mainly helped preserve the particle distribution present at the moment of freezing.

The initial microstructure of the green body MXene-Cu samples shows that the visible MXene increased with MXene loading (Figure 4.2). The dark regions on the sample surface may indicate that MXene appears on and between the Cu grains. While additional characterization is required to confirm that the dark regions are MXenes, the presence can be used as a cautious indication of MXene. In addition,

copper-to-copper contact can still be observed, which is important to enable the particles to bond during sintering. After sintering the grains appears to become encapsulated by an unknown material (Figure 4.3). An EDS analysis on the general microstructure of the 2.5 wt.% MXene-Cu sample, found that the present elements are O, Al, Ti, Cu and F (Figure 4.8). The elemental mapping shows one Cu-rich site and traces of Cu for the remaining site. In addition, the elemental mapping shows O/Al-rich regions on the grains and spatially separated Ti-rich regions between the grains. This indicates that the grains become encapsulated by Al/O-rich material and separated by Ti-rich regions after sintering for the 2.5 wt.% MXene-Cu sample.

In terms of sliding durability and mean CoF, the green body MXene samples performed better than the corresponding sintered samples (Figure 4.18). The composites exhibited improved sliding durability, as both composites finished the tribological measurements. When comparing the mean CoF for the green body to the corresponding sintered composite, the 0.5 wt.% MXene composite went down from 0.949 to 0.661 (Table 4.3). The corresponding improvement for the 1 wt.% MXene composite was from 0.877 to 0.411 (Table 4.3). Among all the samples that finished the tribological measurement, the green body 1 wt.% MXene composite exhibited the lowest mean CoF. To better understand why the pressed samples exhibited improved tribological performance, EDS was performed on the wear tracks of both pressed and sintered MXene-Cu samples. The green body showed a lower oxygen signal in the wear track region (Figure 4.11), when comparing with the elemental mapping opf the wear tracks from the sintered samples (Figure 4.12, Figure 4.8). Apart from this difference, the detected elements and their spatial distributions were relatively similar between the pressed and sintered samples. This suggests that the improved tribological performance of the pressed samples cannot be explained by a clearly different elemental distribution in the wear track alone. However, the lower oxygen signal may indicate less oxidation or fewer oxide-rich regions in the contact area, which could have influenced the frictional response.

After the tribological measurements, the morphology at the wear track differs from

the initial surface microstructure. The SEM images of the wear track on the MXene-Cu samples shows the formation of regions with compacted or smoothed out layers (Figure 4.6).

5.4 Evidence of tribofilm formation

In this thesis, evidence that would support the formations of a tribolayer is the presence of oxide species originating from the sample, MXene derived species and a higher concentration of MXenes at the wear track compared to the sample surface in general.

SEM shows flattened, compacted or smoothed out regions in the wear tracks. This indicates that some component on the sample surface has been smeared or smoothed out at the sliding contact. The morphology of the wear tracks may suggest the formation of a surface layer. These characteristics is extra prominent in the SEM image of the 1 wt.% MXene-Cu sample (Figure 4.6b).

Elemental mapping of the wear track region using EDS shows that the majority of wear track regions consists mainly of Cu, with traces of O, C, Al, F and Ti (Figure 4.14, 4.12, 4.11). This does not support a MXene-derived tribofilm formation at the wear track. The surface layer formation seem in the SEM images might instead be due to for example plastic deformation of Cu particles. One notable sample is the 2.5 wt.% MXene-Cu sample, as the elemental mapping of it's wear track region shows Ti-rich regions (Figure 4.14). Local Ti-rich regions may suggest possible MXene-rich regions at the sliding contact. When specific part of the elemental map annotated "Flat Region" also shows that this particular flattened region is dominated by Ti. However, the CoF remained high during sliding distance (Figure 4.16). This indicates that the potential MXenes present, did not form a continuous lubricating tribofilm.

The wear tracks may contain tribologically modified surface layers, but the available EDS and CoF data do not confirm that these layers were continuous, MXene-rich,

or sufficiently lubricating.

5.5 Comparison between MXene-Cu, Graphene-Cu and Hybrid composites

This section compares the tribological performance for the three sample groups: MXene-Cu, Graphene-Cu and hybrid composites.

When comparing the overall CoF behavior of the sample groups, the mean CoF ranged from 0.62 to 0.949 for the MXene-Cu samples, from 0.869 to 0.929 for the hybrid samples and from 0.78 to 0.857 for the Graphene-Cu samples (Table 4.3, 4.4). While the 2 wt.% MXene sample showed the lowest individual mean CoF, the MXene-Cu sample group had the largest variation in mean CoF among the three sample groups. Graphene-Cu showed a more consistently low mean CoF compared to the other sample groups. When studying the evolution of the CoF during sliding distance, the Graphene-Cu samples also exhibited the smoothest evolution of CoF (Figure 4.19b). The overall lower mean CoF and the its smooth evolution during sliding cycles, suggest a more stable CoF. Hybrid samples did not show an overall lower CoF compared to the single-reinforcement systems.

In terms of sliding durability, the lowest loading MXene sample failed but the corresponding hybrid and Graphene sample finished the measurements (Table 4.3, Table 4.4). This indicates that the graphene containing samples are more stable at low reinforcement loading compared to the MXene-Cu sample. Although an enhanced sliding durability was observed at a lower hybrid loading, the 1 wt.% MXene + 1 wt.% Graphene sample was interrupted early on in the measurement due to excessive friction (Figure 4.19a). While the highest loading hybrid sample failed at an early stage, the MXene-Cu and Graphene-Cu samples achieved their lowest mean COF at 2 wt.% loading.

When comparing the mean wear track width observed for the sample groups, the mean wear track width ranged from 770 µm to 1282 µm for the MXene-Cu sam-

ples, from 854 µm to 1624 µm for the hybrid samples, and from 771 µm to 829 µmfor the Graphene-Cu samples (Table 4.2). While the Graphene-Cu samples exhibited a consistently narrower wear track width range, the hybrid samples exhibited the broadest wear track width range.

The wear track morphology differs between the systems. The optical microscope of the Graphene-Cu samples shows that the wear track has more silvery-gray regions (Figure 4.5) than the golden or dark color observed for the MXene-Cu samples (Figure 4.4). The SEM analysis of the wear track morphology also differs between the sample groups. The wear track of the MXene containing samples shows more characteristics of plastic deformation and smearing (Figure 4.6). The wear track of the Graphene-Cu samples showed more abrasive features (Figure 4.7). This could indicate that the surface was less dominated by ductile deformation when graphene was used as the reinforcement phase. Based on the SEM images, the dominant wear mechanism differed depending the the reinforcement phase.

The hybrid samples did not show lower CoF than MXene-Cu or Graphene-Cu samples nor a narrower wear track (Table 4.4, 4.2). The high-loading hybrid failed while the corresponding loadings did their best at that loading. Based on the collected data, no synergistic effect can be observed for the hybrid samples.

The sample group that appears to be the most promising in terms of enhancing the tribological performance of Cu is purely reinforcing the Cu matrix with graphene. This is based on the sliding durability at low loading, consistently low mean CoF and smooth evolution of CoF during sliding distance.

5.6 Effect of surface polishing

This section will discuss the effect of surface polishing on the general microstructure of the samples and the tribological behavior. Polishing was investigated to get a better understanding of how the surface condition effect the tribological performance of the samples. Polishing did not have a universal effect on the samples. Instead,

the response depended on the sample composition.

The mean CoF of 2 wt.% MXene-Cu sample increased after polishing by approximately 0.25 (Table 4.3). Polishing the sample surface did not result in a friction improvement. In addition, the mean wear track width increased by approximately 700 µm (Table 4.2). The broad wear track width may indicate that there was no improvement in wear damage when comparing to the other MXene-Cu samples.

After polishing the 2.5 wt.% MXene-Cu sample, a slight friction improvement of a decrease in mean CoF by approximately 0.1 could be observed (Table 4.3). A well-defined wear track could also be observed on the polished sample surface after the tribological measurement. However, the mean wear track width of the polished sample was relatively broad compared to the other MXene-Cu samples (Table 4.2). After polishing the tribological performance of 2.5 wt.% MXene improved as the CoF decreased and a well-defined wear track could be observed. Before polishing, the sample surface is dominated by O/Al rich regions that are spatially separated by Ti-rich regions (Figure 4.8). However, after polishing the surface mainly consists of homogeneously distributed Cu, C, F with traces of O, Ti, and Al (Figure 4.9). The polishing also changes the elemental composition of the wear track where Cu, O and Fe dominates at the wear track instead of O, Al, and Ti before polishing (Figure 4.14, 4.15). Based on the elemental mapping more Ti was exposed before the polishing, indicating that MXenes were present at the contact area. However, after polishing there is only small traces of Ti present. The EDS analysis does not support that the lubrication mechanisms that resulted in a lower CoF was driven by MXenes.

Among the MXene-Cu samples, the broadest mean wear track widths were observed for the polished MXene-Cu samples. This indicates that the elements present on the 2 wt.% MXene-Cu sample surface was not beneficial for lubrication and polishing helped.

The mean CoF of the 0.25 wt.% MXene + 0.25 wt.% Graphene increased after pol-

ishing by approximately 0.03 (Table 4.4). Polishing the sample surface did not result in a friction improvement. In addition, the wear track width increased by approximately 400 µm (Table 4.2). The increase in mean wear track width may indicate that polishing the sample surface, did not result in an improvement in wear damage.

The CoF of the highest loading hybrid samples decreased by approximately 0.5 (Table 4.4) and the sample now finished the measurement after polishing (Figure 4.20a). This indicates friction improvement as both the CoF decreased and the sliding durability increased. The wear track width increased by approximately 650 µm (Table 4.2). This does not indicate an improvement in wear damage.

The mean CoF of Graphene-Cu samples increased after polishing (Table 4.4). After polishing the wear track width of graphene containing samples increased significantly (Table 4.2). More specifically, polishing worsened the tribological performance of the 1 wt.% Graphene-Cu sample both regarding the mean CoF and the mean wear track width.

While polishing was beneficial for the 2.5 wt.% MXene-Cu sample, it might have removed a beneficial surface layer or changed the contact conditions for the 1 wt.% Graphene-Cu sample.

5.7 Limitations and uncertainties

Limitations of the tribological testing includes a limited number of repeats, difficulties regarding comparing samples that did not complete the full measurement, and the use of wear track width.

The tribological measurement was performed once per sample. With the exception of 1 wt.% MXene + 1 wt.% Graphene that was measured twice at different spots on the same sample (Figure 4.21). The results from the measurements are similar, both measurements were interrupted at early stages in the measurement due to excessive friction and exhibited a relatively high mean CoF (Table 4.4). The differ-

ences suggest that local variations in surface or microstructure within one sample might affect the tribological response. Thus, the limited number of repeats for each sample makes it more difficult to discuss small differences between samples. The measurement variation seen from the same sample does add uncertainties to the results and makes it more difficult to discuss small differences between the samples. Consequently, this also adds uncertainty to the possible conclusions that can be drawn reliably from this thesis. Furthermore, not all samples completed the full tribological measurement, making it hard to compare other potential metrics of the tribological performance such as the morphology of the wear track or the mean wear track width. Additionally, using the wear track width as an indication of the wear adds some uncertainty to the discussion as the wear track width does not always fully describe material loss. A more reliable way to quantify the wear is to use the wear track volume.

Another uncertainty is related to the samples. The EDS analysis both from the wear track area and the microstructure in general of the 2.5 wt.% MXene-Cu sample shows high content of Al (Figure 4.8). This is especially notable for the agglomerates that mostly consist of Al and O. For the polished 2.5 wt.% MXene-Cu sample (Figure 4.9) or the green body 1 wt.% MXene-Cu sample (Figure 4.11), the Al contents are lower but still there. Some possible sources of the Al is contamination, especially from the pressing step, or that the Al present in the MAX phase was not fully etched away during the etching. However, the EDS mapping of the 0.5 wt.% Graphene-Cu sample (Figure 4.10) does not show the presence of Al. This may suggest that the Al is not from contamination during pressing, as contamination likely would be present independent of reinforcement phase, but instead might be present due to incomplete etching of the MAX phase.

One limitation related to the use of EDS is that EDS cannot confirm the presence of MXene by itself. It can detect Ti-rich region that can be used as an indication. The samples contain a relatively low loading of reinforcement phase, this can make it difficult for the EDS to detect the low signals from the reinforcement phase. A

second limitation with EDS is that it cannot identify the chemical phases only the present elements. After detecting Ti-rich regions, the EDS cannot distinguish between intact MXene, Ti-oxide, or another Ti-containing phase.

One limitation to be aware of is related to the use of SEM images. While they can show the morphology of the wear track, it cannot confirm tribofilm formation. It can be used as an indication or suggest the formation of a surface layer but it cannot say anything about the chemistry or lubricating function of the layer.

5.8 Implications for electrical switching applications

This section aims to discuss whether MXene-Cu composites are promising for electrical switching applications.

The MXene-Cu composites exhibit improved sliding durability compared to the pure Cu reference (Figure 4.16). However, a major limitation to the composites is the high CoF (Table 4.3). Based on the results acquired in this thesis, the composites cannot be considered a direct replacement to grease or oil lubrication. While MXene-Cu composites exhibit increased sliding durability, their CoF is nowhere near the CoF for the greased reference. Based on the composite loadings that were investigated, the 2 wt.% MXene loading shows the largest potential for future optimization as it achieved a low initial CoF (Figure 4.16). Before a practical application of MXene-Cu composites in electrical switching devices, a stable low-friction and low-wear behavior is required over longer testing periods. In addition, the green body 1 wt.% MXene sample exhibits a lower CoF with stable evolution during sliding distance (Figure 4.18. These observations indicate that more information about processing is required before practical application. Since the application is electrical switching, future work also needs to evaluate to electrical performance after wear.

Reinforcing the Cu metal matrix with MXenes shows potential for tribological enhancement, but further material and process optimization is required before a prac-

tical application is relevant.

6
Conclusion

This thesis investigated whether MXene reinforcement can improve the tribological performance of copper matrix composites for electrical switching applications. The results show that reinforcing Cu with MXene improved sliding durability, meaning the material's ability to sustain sliding contact compare to the pure Cu reference. The MXene-Cu composites lasted longer and completed their tribological measurements, compared to the pure Cu reference that was interrupted at an early stage due to excessive friction. Therefore, MXene reinforcement showed potential for improving the sliding durability of Cu. However, not all MXene-Cu composites achieved a sustained reduction in coefficient of friction under the tested conditions. Instead, the measured CoF remained relative high for most MXene-Cu composites. Some MXene-Cu composites showed potential, namely the 2 wt.% MXene-Cu sample, the polished 2.5 wt.% MXene-Cu sample and the green body 1 wt.% MXene-Cu sample. The 2 wt.% MXene-Cu composite exhibited the lowest mean CoF among the sintered MXene-Cu samples and maintained a CoF below 0.5 during the initial sliding distance. However, this low-friction behavior was not sustained throughout the full measurement. The polished 2.5 wt.% MXene-Cu sample achieved a mean CoF of 0,788. Most notably, the green body 1 wt.% MXene-Cu sample achieved a stable evolution of CoF during sliding distance and a mean CoF of 0.411.

The tribological response appeared to be strongly dependent on MXene loading. The 0.5 wt.% MXene-Cu composite showed poor performance, with high CoF, an interrupted measurement, and a broad wear track. Although increasing the MXene content improved the sliding durability, the highest loading of 2.5 wt.% MXene did not result in the best performance. Instead, the 2.5 wt.% MXene-Cu sample exhibited a high CoF and an irregular wear-track morphology. This indicates that a

higher MXene loading does not automatically improve the tribological performance, and that intermediate loadings appear more promising for further optimization.

The microstructural and elemental analyses suggest that the observed wear behavior was mainly governed by plastic deformation, material smearing, and the formation of compacted surface layers. Although SEM images indicated the possible formation of tribologically modified surface layers, the EDS analysis did not confirm the formation of a continuous MXene-derived lubricating tribofilm. Local Ti-rich regions were observed for the 2.5 wt.% MXene-Cu sample, but these regions did not result in stable low-friction behavior.

The results also showed that freeze-drying impacted the microstructure and dispersion of MXene in the copper matrix by preserving the particle distribution created during slurry mixing. Rapid freezing and freeze-drying can be considered a useful preservation step, as the risk of density-driven segregation and drying-induced agglomeration is reduced. However, the dispersion depends heavily on achieving a homogeneous slurry before freezing.

The comparison with graphene-containing composites showed that Graphene-Cu composites exhibited more consistent friction behavior and narrower wear track width ranges than both MXene-Cu and MXene-Graphene-Cu hybrid composites. The hybrid composites did not show a clear synergistic effect, as they did not achieve lower CoF or narrower wear tracks than the single-reinforcement systems. In addition, the green body MXene-Cu samples showed lower CoF than their corresponding sintered samples, indicating that processing route and surface condition strongly influence the tribological response.

Overall, MXene reinforcement showed potential for improving the sliding durability of Cu, but did not provide stable low-friction behavior under the investigated conditions. Therefore, the investigated MXene-Cu composites cannot currently be considered a direct replacement for oil- or grease-based lubrication in electrical switching

applications. Further optimization of MXene loading, processing conditions, and surface preparation is required. Future work should also include repeated tribological measurements, wear volume analysis, and evaluation of electrical performance after sliding.

A

Additional Optical Microscopy Images

A.1 Effect of Surface Polishing

Figure A.1 shows optical microscopy images of selected composite surfaces before and after polishing. The included samples are 2.5 wt.% MXene-Cu, 1 wt.% MXene-Graphene-Cu, and 1 wt.% Graphene-Cu.

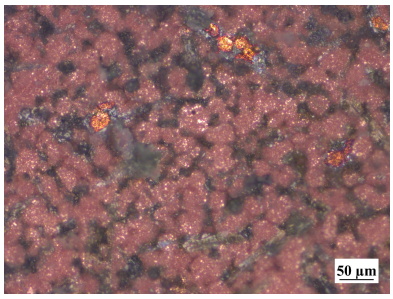

(a) Sintered 2.5 wt.% MXene-Cu surface before polishing.

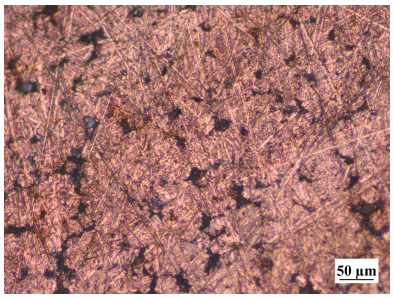

(b) Sintered 2.5 wt.% MXene-Cu surface after polishing.

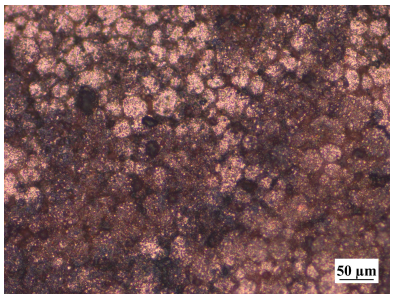

(c) Sintered 1 wt.% MXene-Graphene-Cu surface before polishing.

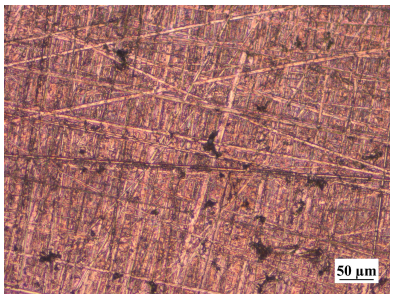

(d) Sintered 1 wt.% MXene-Graphene-Cu surface after polishing.

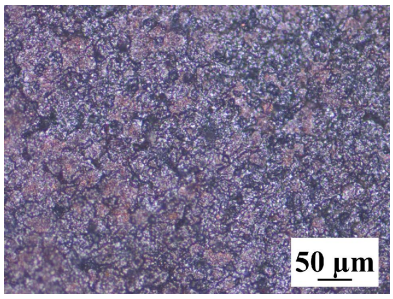

(e) Sintered 1 wt.% Graphene-Cu surface before polishing.

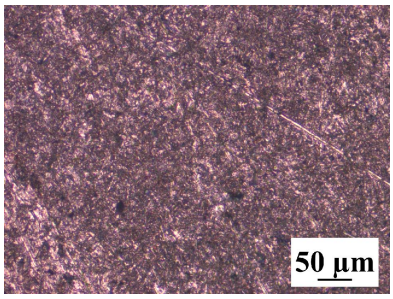

(f) Sintered 1 wt.% Graphene-Cu surface after polishing.

Figure A.1: Optical microscopy images of selected composite surfaces before and after polishing.

B

Additional Wear Track Images

B.1 SEM Images of MXene-Graphene-Cu Wear Tracks

Figure B.1 shows additional SEM images of selected MXene-Graphene-Cu wear tracks after tribological testing.

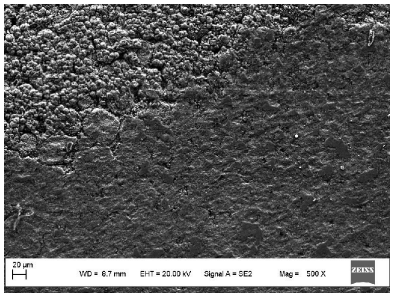

(a) 0.25 wt.% MXene-Graphene-Cu wear track at 500× magnification.

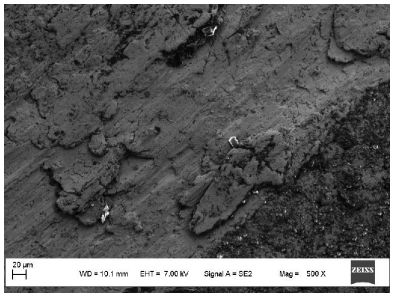

(b) 1 wt.% MXene-Graphene-Cu wear track at 500× magnification.

Figure B.1: SEM images of selected MXene-Graphene-Cu wear tracks after tribological testing.

B.2 Optical Microscopy Images of MXene-Graphene-Cu Wear Tracks

Figure B.2 shows optical microscopy images of the wear tracks after tribological testing for the MXene-Graphene-Cu composites. The included loadings are 0.25 wt.% MXene + 0.25 wt.% graphene, 0.5 wt.% MXene + 0.5 wt.% graphene, and 1 wt.% MXene + 1 wt.% graphene.

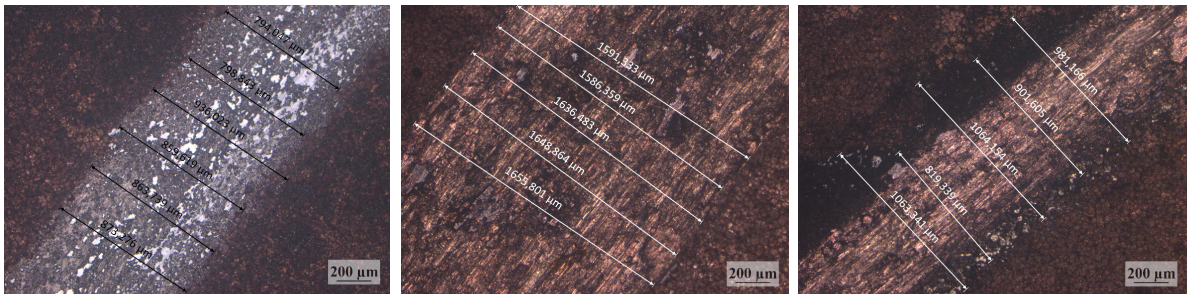

(a) 0.25 wt.% MXene + 0.25 wt.% graphene wear track.

(b) 0.5 wt.% MXene + 0.5 wt.% graphene wear track.

(c) 1 wt.% MXene + 1 wt.% graphene wear track.

Figure B.2: Optical microscopy images of wear tracks after tribological testing on MXene-Graphene-Cu composites.

B.3 Optical Microscopy Images of Polished MXene-Cu Wear Tracks

Figure B.3 shows optical microscopy images of wear tracks after tribological testing on polished MXene-Cu composite surfaces. The included MXene loadings are 2 wt.% and 2.5 wt.%.

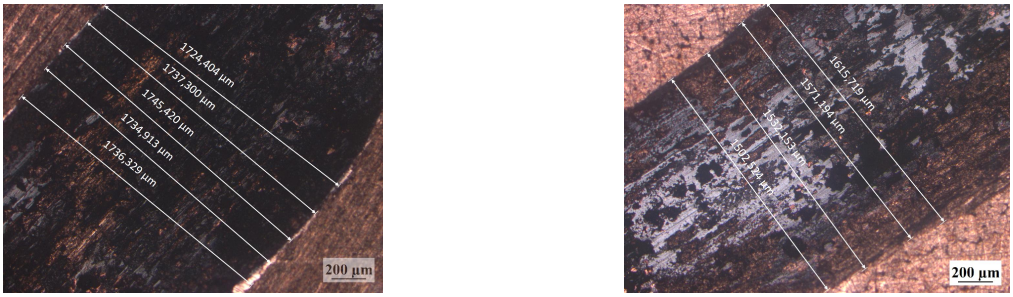

(a) Polished 2 wt.% MXene-Cu wear track.

(b) Polished 2.5 wt.% MXene-Cu wear track.

Figure B.3: Optical microscopy images of wear tracks after tribological testing on polished MXene-Cu composite surfaces.

B.4 Optical Microscopy Images of Polished Graphene-Containing Wear Tracks

Figure B.4 shows optical microscopy images of wear tracks after tribological testing on polished graphene-containing composite surfaces. The included samples are 0.25 wt.% MXene + 0.25 wt.% graphene, 1 wt.% MXene + 1 wt.% graphene, and 1 wt.%

Graphene-Cu.

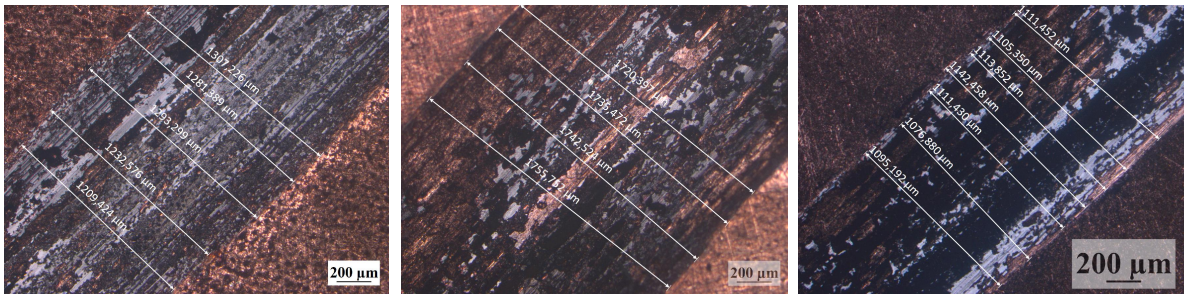

(a) Polished 0.25 wt.% MXene + 0.25 wt.% graphene wear track.

(b) Polished 1 wt.% MXene + 1 wt.% graphene wear track.

(c) Polished 1 wt.% Graphene-Cu wear track.

Figure B.4: Optical microscopy images of wear tracks after tribological testing on polished graphene-containing composite surfaces.

C

Additional Tribological Measurements

C.1 Effect of Surface Polishing on Graphene-Containing Cu Composites

Figure C.1 compares the CoF evolution of graphene-containing Cu composite samples before and after surface polishing. Prior to tribological testing, the samples were polished using abrasive paper, as described in Section 3.4.1.

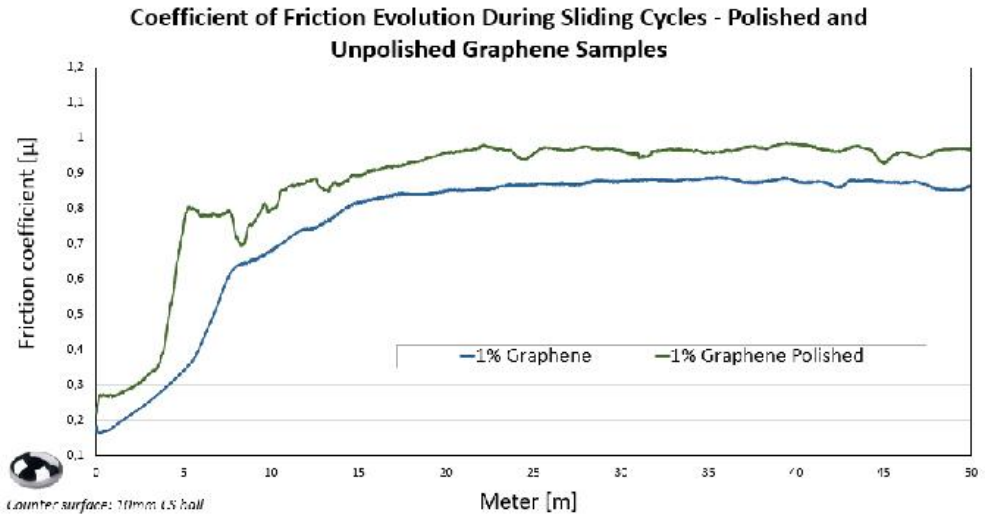

Figure C.1: Comparison of CoF evolution before and after surface polishing for graphene-containing Cu composites.

C.2 Effect of Sintering on the Friction Behavior of Graphene-Containing Cu Composites

Figure C.2 compares the CoF evolution of sintered and green body graphene-containing Cu composites.

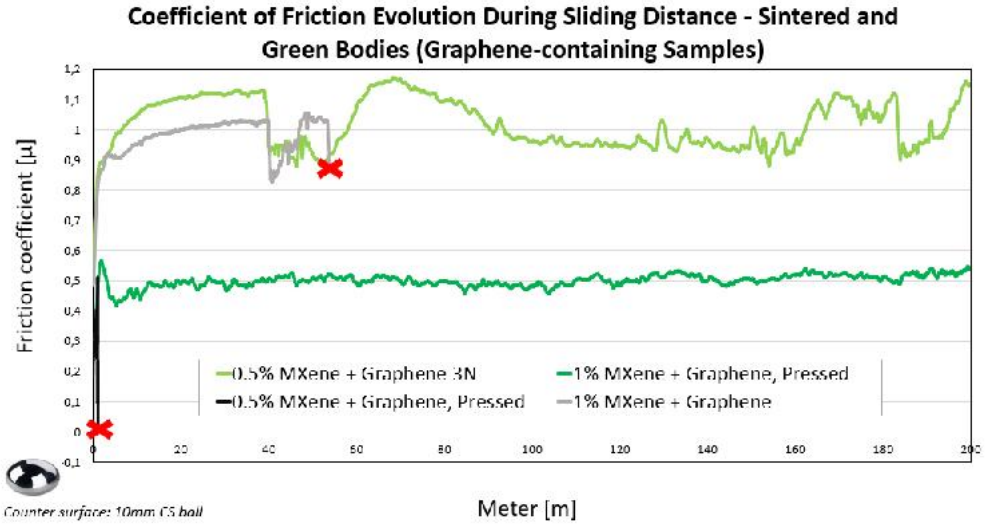

Figure C.2: Comparison of CoF evolution between green body and sintered graphene-containing Cu composites.

References

[1] Joseph R. Davis, ed. *Copper and Copper Alloys*. ASM Specialty Handbook. ASM International, 2001. ISBN: 978-0-87170-726-0.

[2] Yu Dai et al. "Evolution of the mechanical and tribological properties of copper matrix composites reinforced with Ni-coated HfCxNy particles". In: *Journal of Alloys and Compounds* 1040 (2025), p. 183647. ISSN: 0925-8388. DOI: https://doi.org/10.1016/j.jallcom.2025.183647. URL: https://www.sciencedirect.com/science/article/pii/S0925838825052089.

[3] Wen-Jing Zhang et al. "Researches for higher electrical conductivity copper-based materials". In: *cMat* 1.1 (2024), e13. DOI: https://doi.org/10.1002/cmt2.13. eprint: https://onlinelibrary.wiley.com/doi/pdf/10.1002/cmt2.13. URL: https://onlinelibrary.wiley.com/doi/abs/10.1002/cmt2.13.

[4] Diana Berman, Ali Erdemir, and Anirudha V. Sumant. "Graphene: a new emerging lubricant". In: *Materials Today* 17.1 (2014), pp. 31–42. ISSN: 1369-7021. DOI: https://doi.org/10.1016/j.mattod.2013.12.003. URL: https://www.sciencedirect.com/science/article/pii/S1369702113004574.

[5] Vineet Kumar and Anchal Singh. "A comprehensive review of processing techniques, reinforcement effects, and performance characteristics in copper-based metal matrix composites". In: *Interactions* 245.357 (2024). ISSN: 3005-0731. DOI: https://doi.org/10.1007/s10751-024-02200-9. URL: https://link.springer.com/article/10.1007/s10751-024-02200-9.

[6] Michael Naguib et. al. "Two-Dimensional Nanocrystals Produced by Exfoliation of Ti3AlC2". In: *Advanced Materials* 23.37 (2011). ISSN: 0935-9648. DOI: https://doi.org/10.1002/adma.201102306. URL: https://advanced.onlinelibrary.wiley.com/doi/10.1002/adma.201102306.

[7] Maaz Ullah Khan et al. "Preparations and Applications of MXene–Metal Composites: A Review". In: *Coatings* 12.4 (2022). ISSN: 2079-6412. DOI: 10.3390/coatings12040516. URL: https://www.mdpi.com/2079-6412/12/4/516.

[8] Km. Pooja, Nazia Tarannum, and Pallavi Chaudhary. "Metal matrix composites: revolutionary materials for shaping the future". In: *Discover Materials* 5.1 (2025). ISSN: 2730-7727. DOI: 10.1007/s43939-025-00226-6. URL: https://link.springer.com/article/10.1007/s43939-025-00226-6.

[9] MFA Ho J. D. *Switches*. URL: https://www.ebsco.com/research-starters/engineering/switches. (accessed: 06.17.2026).

[10] M. MADEJ. "SILVER– BASED INFILTRATED COMPOSITES". In: *Archives of metallurgy and materials* 57 (2 2012). DOI: 10.2478/v10172-012-0064-x.

URL: https://www.researchgate.net/publication/273249110_Silver_-_Based_Infiltrated_Composites.

[11] N.K. Myshkin. "Tribological problems in electrical contacts". In: *Tribology International* 24.1 (1991), pp. 45–49. ISSN: 0301-679X. DOI: https://doi.org/10.1016/0301-679X(91)90062-E. URL: https://www.sciencedirect.com/science/article/pii/0301679X9190062E.

[12] Bharat Bhushan. "Introduction". In: *Introduction to Tribology*. John Wiley Sons, Ltd, 2013. Chap. 1, pp. 1–8. ISBN: 9781118403259. DOI: https://doi.org/10.1002/9781118403259.ch1. eprint: https://onlinelibrary.wiley.com/doi/pdf/10.1002/9781118403259.ch1. URL: https://onlinelibrary.wiley.com/doi/abs/10.1002/9781118403259.ch1.

[13] EBSCO. *Friction*. URL: https://www.ebsco.com/research-starters/engineering/friction. (accessed: 05.15.2026).

[14] Ahmed Abdelbary and Li Chang. "4 - Friction and wear". In: *Principles of Engineering Tribology*. Academic Press, 2023, pp. 127–206. ISBN: 978-0-323-99115-5. DOI: https://doi.org/10.1016/B978-0-323-99115-5.00011-6. URL: https://www.sciencedirect.com/science/article/pii/B9780323991155000116.

[15] Society of Tribologists and Lubrication Engineers. *Introduction to Tribology*. URL: https://www.stle.org/files/What_is_tribology/Tribology_Wear.aspxn. (accessed: 05.15.2026).

[16] Ernest Rabinowicz. "Abrasive and Other Types of Wear". In: *Friction and wear of materials*. Wiley, 1965. Chap. 7, pp. 167–197. ISBN: 9781118403259. URL: https://archive.org/details/frictionwearofma00rabi/page/n9/mode/2up.

[17] H. Dong. "3 - Tribological properties of titanium-based alloys". In: *Surface Engineering of Light Alloys*. Ed. by Hanshan Dong. Woodhead Publishing Series in Metals and Surface Engineering. Woodhead Publishing, 2010, pp. 58–80. ISBN: 978-1-84569-537-8. DOI: https://doi.org/10.1533/9781845699451.1.58. URL: https://www.sciencedirect.com/science/article/pii/B9781845695378500038.

[18] Nam P. Suh. "An overview of the delamination theory of wear". In: *Wear* 44.1 (1977), pp. 1–16. ISSN: 0043-1648. DOI: https://doi.org/10.1016/0043-1648(77)90081-3. URL: https://www.sciencedirect.com/science/article/pii/0043164877900813.

[19] Alvine Pitman Brooks and Duranty Roosendaal Simmons. *Preliminary Test Methodology for Linear Reciprocating Ball-on-Flat In situ Friction and Wear Studies of Polymers in High Pressure Hydrogen*. Tech. rep. PNNL-SA-26121. Richland, Washington: Pacific Northwest National Laboratory, Dec. 2016. URL: https://h2tools.org/sites/default/files/PNNL%20Preliminary%20Test%20Methodology%20Report%2012-22-16.pdf (visited on 06/08/2026).

[20] Jun Qu and John J. Truhan. "An efficient method for accurately determining wear volumes of sliders with non-flat wear scars and compound curvatures". In: *Wear* 261.7 (2006), pp. 848–855. ISSN: 0043-1648. DOI: https://doi.org/10.1016/j.wear.2006.01.009. URL: https://www.sciencedirect.com/science/article/pii/S0043164806000147.

[21] Ashgar Shirani et. al. “Tribocatalytically-activated formation of protective friction and wear reducing carbon coatings from alkane environment”. In: *Scientific Reports* 11.1 (2021). ISSN: 2045-2322. DOI: https://doi.org/10.1038/s41598-021-00044-9. URL: https://www.nature.com/articles/s41598-021-00044-9.

[22] Lei Qiao et al. “Effects of Sliding Speed on Wear Behavior of High-Velocity Oxygen Fuel-Sprayed FeCrMoNiCuBSiC Metallic Glass Coatings”. In: *Lubricants* 13.1 (2025). ISSN: 2075-4442. DOI: 10.3390/lubricants13010010. URL: https://www.mdpi.com/2075-4442/13/1/10.

[23] Philipp Maximilian Sieberg, Dzhem Kurtulan, and Stefanie Hanke. “Wear Mechanism Classification Using Artificial Intelligence”. In: *Materials* 15.7 (2022). ISSN: 1996-1944. DOI: 10.3390/ma15072358. URL: https://www.mdpi.com/1996-1944/15/7/2358.

[24] Michael Khonsari and E.R. Booser. *Low Temperature and Viscosity Limits*. URL: https://www.machinerylubrication.com/Read/1014/low-temperature-viscosity-limits. (accessed: 05.15.2026).

[25] Md Rahatul Islam Sazzad et al. “Advancing sustainable lubricating oil management: Re-refining techniques, market insights, innovative enhancements, and conversion to fuel”. In: *Heliyon* 48.20 (2024), e39248. ISSN: 2405-8440. DOI: https://doi.org/10.1016/j.heliyon.2024.e39248. URL: https://www.sciencedirect.com/science/article/pii/S2405844024152796.

[26] Kenneth Holmberg and Ali Erdemir. “The impact of tribology on energy use and CO2 emission globally and in combustion engine and electric cars”. In: *Tribology International* 135 (2019), pp. 389–396. ISSN: 0301-679X. DOI: https://doi.org/10.1016/j.triboint.2019.03.024. URL: https://www.sciencedirect.com/science/article/pii/S0301679X19301446.

[27] T. W. Scharf and S. V. Prasad. “Solid lubricants: a review”. In: *Journal of Materials Science* 10 (2013), pp. 511–531. ISSN: 1573-4803. DOI: https://doi.org/10.1007/s10853-012-7038-2. URL: https://link.springer.com/article/10.1007/s10853-012-7038-2.

[28] International Copper Association. *Copper Attributes and Alloys*. URL: https://internationalcopper.org/sustainable-copper/about-copper/copper-attributes-and-alloys/. (accessed: 05.15.2026).

[29] Dean McClements and Dr. Mahder Tewolde. *6 of the Most Ductile Metals*. URL: https://www.xometry.com/resources/materials/most-ductile-metal/. (accessed: 05.15.2026).

[30] Marcin Kargul and Marek Konieczny. “Copper matrix composites reinforced with steel particles”. In: *AIMS Materials Science* 8.3 (2021), pp. 321–342. DOI: 10.3934/matersci.2021021.

[31] Alexey Moshkovich et al. “Friction, wear and plastic deformation of Cu and / brass under lubrication conditions”. In: *Wear* 320 (2014), pp. 34–40. ISSN: 0043-1648. DOI: https://doi.org/10.1016/j.wear.2014.08.016. URL: https://www.sciencedirect.com/science/article/pii/S0043164814002749.

[32] Xiaotao Li et al. “Trade-off model for strength-ductility relationship of metallic materials”. In: *Acta Materialia* 289 (Mar. 2025), p. 120942. DOI: 10.1016/j.actamat.2025.120942.

[33] Bhavin N. Vadgama, Robert L. Jackson, and Daniel K. Harris. "Molecular scale analysis of dry sliding copper asperities". In: *Applied Nanoscience* 5.4 (2015), pp. 469–480. ISSN: 2190-5517. DOI: 10.1007/s13204-014-0339-9. URL: https://doi.org/10.1007/s13204-014-0339-9.

[34] Andreas Rosenkranz et al. "Perspectives of 2D MXene Tribology". In: *Advanced Materials* 35.5 (2023), p. 2207757. DOI: https://doi.org/10.1002/adma.202207757. eprint: https://advanced.onlinelibrary.wiley.com/doi/pdf/10.1002/adma.202207757. URL: https://advanced.onlinelibrary.wiley.com/doi/abs/10.1002/adma.202207757.

[35] M. K. Singh, G. Ji, V. Kumar, et al. "Sustainable development of copper matrix hybrid composites using waste stainless steel chips: a physical and tribological investigation". In: *Scientific Reports* 16.1 (2026). ISSN: 2045-2322. DOI: 10.1038/s41598-026-42090-1. URL: https://www.nature.com/articles/s41598-026-42090-1.

[36] Li CS. Zhang FX Chu YQ. "Fabrication and Tribological Properties of Copper Matrix Solid Self-Lubricant Composites Reinforced with Ni/NbSe2 Composites." In: *Materials (Basel).* 12.11 (2019). DOI: 10.3390/ma12111854.. URL: https://pmc.ncbi.nlm.nih.gov/articles/PMC6600960/.

[37] MIT Open Learning Library. *Lecture 20: Structure 3: Strengthening Mechanisms and Surface Energy.* https://openlearninglibrary.mit.edu/assets/courseware/v1/e681247bcbdf741133f950a6a41caa12/asset-v1:MITx+3.012S.3x+1T2019+type@asset+block/3012_Strengthening_and_Surface_Energy_reduced.pdf. Course material for MITx 3.012S.3x. Accessed: 2026-06-18.

[38] Chandra Shekhar et al. "Recent Progress in Particulate Reinforced Copper-Based Composites: Fabrication, Microstructure, Mechanical, and Tribological Properties—A Review". In: *Advanced Engineering Materials* 27.2 (2025), p. 2401748. DOI: https://doi.org/10.1002/adem.202401748. eprint: https://advanced.onlinelibrary.wiley.com/doi/pdf/10.1002/adem.202401748. URL: https://advanced.onlinelibrary.wiley.com/doi/abs/10.1002/adem.202401748.

[39] Max Marian et al. "Layered 2D Nanomaterials to Tailor Friction and Wear in Machine Elements—A Review". In: *Advanced Materials Interfaces* 9.3 (2022), p. 2101622. DOI: https://doi.org/10.1002/admi.202101622. URL: https://advanced.onlinelibrary.wiley.com/doi/abs/10.1002/admi.202101622.

[40] Maryam A. Saeed et al. "Graphene Applications in Composites, Energy, and Water Treatment". In: *Macromolecular Materials and Engineering* 310.4 (2025), p. 2400316. DOI: https://doi.org/10.1002/mame.202400316. URL: https://onlinelibrary.wiley.com/doi/abs/10.1002/mame.202400316.

[41] Jianlin Sun and Shaonan Du. "Application of graphene derivatives and their nanocomposites in tribology and lubrication: a review". In: *RSC Adv.* 9 (69 2019), pp. 40642–40661. DOI: 10.1039/C9RA05679C. URL: http://dx.doi.org/10.1039/C9RA05679C.

[42] Paloma Hidalgo-Manrique et. al. “Copper/graphene composites: a review”. In: *Journal of Materials Science* 54 (19 2019), pp. 31–42. DOI: 10.1007/s10853-019-03703-5. URL: https://doi.org/10.1007/s10853-019-03703-5.

[43] Martin Dahlqvist, Michel W. Barsoum, and Johanna Rosen. “MAX phases – Past, present, and future”. In: *Materials Today* 72 (2024), pp. 1–24. ISSN: 1369-7021. DOI: https://doi.org/10.1016/j.mattod.2023.11.010. URL: https://www.sciencedirect.com/science/article/pii/S1369702123003577.

[44] Michel W. Barsoum. “The MN+1AXN phases: A new class of solids: Thermodynamically stable nanolaminates”. In: *Progress in Solid State Chemistry* 28.1 (2000), pp. 201–281. ISSN: 0079-6786. DOI: https://doi.org/10.1016/S0079-6786(00)00006-6. URL: https://www.sciencedirect.com/science/article/pii/S0079678600000066.

[45] C. B. Subba et al. “Comprehensive review of MAX phase and MXene materials: synthesis, properties, and applications”. In: *Carbon Letters* 35 (2025), pp. 2485–2570. DOI: 10.1007/s42823-025-00979-3.

[46] etl al. Michael Ghidiu. “Conductive two-dimensional titanium carbide ‘clay’ with high volumetric capacitance”. In: *Nature* 516 (), pp. 2485–2570. DOI: 10.1038/nature13970.

[47] Ubaid Ur Rahman et al. “MXenes as Emerging Materials: Synthesis, Properties, and Applications”. In: *Molecules* 27.15 (2022). ISSN: 1420-3049. DOI: 10.3390/molecules27154909. URL: https://www.mdpi.com/1420-3049/27/15/4909.

[48] Brian C. Wyatt, Srinivasa Kartik Nemani, and Babak Anasori. “2D transition metal carbides (MXenes) in metal and ceramic matrix composites”. In: *Nano Convergence* 8.1 (2021), p. 16. DOI: 10.1186/s40580-021-00266-7. URL: https://link.springer.com/article/10.1186/s40580-021-00266-7.

[49] et. al. Mathew S. “Transition metal oxide/chalcogenide-integrated MXene heterostructures: emerging materials for supercapacitors and water splitting”. In: *Advanced Materials* 6 (2025), pp. 7207–7230. DOI: 10.1039/D5MA00706B. URL: https://pubs.rsc.org/en/content/articlehtml/2025/ma/d5ma00706b?utm.

[50] “Interplay of oxidation and graphitization governs tribological performance in Ni-MXene composites”. In: *Tribology International* 220 (2026), p. 111963. ISSN: 0301-679X. DOI: https://doi.org/10.1016/j.triboint.2026.111963. URL: https://www.sciencedirect.com/science/article/pii/S0301679X26003063.

[51] Junhong Jia et al. “Fabrication, microstructure and properties of Ti3C2Tx MXene nanosheets reinforced Cu composites”. In: *Journal of Materials Research and Technology* 23 (2023), pp. 503–514. ISSN: 2238-7854. DOI: https://doi.org/10.1016/j.jmrt.2022.12.189. URL: https://www.sciencedirect.com/science/article/pii/S2238785422020798.

[52] et. al. Christina Danecker. “Hybrid MXene coatings: unlocking synergistic lubrication properties of Ti3C2Tx and NbCTx MXenes for improved tribological performance”. In: *Scientific Reports* 15 (2025). ISSN: 2045-2322. DOI: https://doi.org/10.1038/s41598-025-32533-6. URL: https://www.nature.com/articles/s41598-025-32533-6.

[53] P. K. Rohatgi, S. Ray, and Y. Liu. "Tribological properties of metal matrix-graphite particle composites". In: *International Materials Reviews* 37.1 (1992), pp. 129–152. DOI: 10.1179/imr.1992.37.1.129. eprint: https://journals.sagepub.com/doi/pdf/10.1179/imr.1992.37.1.129. URL: https://journals.sagepub.com/doi/abs/10.1179/imr.1992.37.1.129.

[54] et. al. Quanpeng Yang. "Effect of surface termination on the balance between friction and failure of Ti3C2Tx MXenes". In: *npj Materials Degradation* 7 (2025). ISSN: 2397-2106. DOI: https://doi.org/10.1038/s41529-023-00326-9. URL: https://www.nature.com/articles/s41529-023-00326-9.

[55] Yi-Fan Yan et al. "Ceramic particles reinforced copper matrix composites manufactured by advanced powder metallurgy: preparation, performance, and mechanisms". In: *International Journal of Extreme Manufacturing* 5.3 (2023), p. 032006. DOI: 10.1088/2631-7990/acdb0b. URL: https://www.sciopen.com/article/10.1088/2631-7990/acdb0b.

[56] Caique Movio Pereira de Souza et al. "Evaluation of Different Blending Methods to Obtain Copper Composites with Graphene Oxide". In: *Metals* 14.11 (2024). ISSN: 2075-4701. DOI: 10.3390/met14111279. URL: https://www.mdpi.com/2075-4701/14/11/1279.

[57] Jakob Beirowski et al. "Freeze-drying of nanosuspensions, 1: freezing rate versus formulation design as critical factors to preserve the original particle size distribution". In: *Journal of Pharmaceutical Sciences* 100.5 (2011), pp. 1958–1968. DOI: 10.1002/jps.22425.

[58] Lei Qian and Haifei Zhang. "Controlled freezing and freeze drying: a versatile route for porous and micro-/nano-structured materials". In: *Journal of Chemical Technology & Biotechnology* 86.2 (2011), pp. 172–184. DOI: https://doi.org/10.1002/jctb.2495. eprint: https://scijournals.onlinelibrary.wiley.com/doi/pdf/10.1002/jctb.2495. URL: https://scijournals.onlinelibrary.wiley.com/doi/abs/10.1002/jctb.2495.

[59] Nicky Savjani et al. "Tribology of Copper Metal Matrix Composites Reinforced with Fluorinated Graphene Oxide Nanosheets: Implications for Solid Lubricants in Mechanical Switches". In: *ACS Applied Nano Materials* 6.10 (2023), pp. 8202–8213. DOI: 10.1021/acsanm.3c00399. eprint: https://doi.org/10.1021/acsanm.3c00399. URL: https://doi.org/10.1021/acsanm.3c00399.

[60] Michael Stuer, Zhe Zhao, and Paul Bowen. "Freeze granulation: Powder processing for transparent alumina applications". In: *Journal of the European Ceramic Society* 32.11 (2012), pp. 2899–2908. DOI: 10.1016/j.jeurceramsoc.2012.02.038.

[61] H. Nakajima, T. Ogura, and Y. et al. Kato. "Quantitative evaluation of particle–binder interactions in ceramic slurries via differential centrifugal sedimentation". In: *Scientific Reports* 14 (1 2024). ISSN: 2045-2322. DOI: 10.1038/s41598-024-68420-9. URL: https://www.nature.com/articles/s41598-024-68420-9.

[62] Antoine Thill and Olivier Spalla. "Aggregation due to capillary forces during drying of particle submonolayers". In: *Colloids and Surfaces A: Physicochemical and Engineering Aspects* 217.1 (2003). Symposium C of the E-MRS

2002 Spring Meeting in Strasbourg, France, pp. 143–151. ISSN: 0927-7757. DOI: https://doi.org/10.1016/S0927-7757(02)00569-1. URL: https://www.sciencedirect.com/science/article/pii/S0927775702005691.

[63] de Vries A et al. "Controlling Agglomeration of Protein Aggregates for Structure Formation in Liquid Oil: A Sticky Business." In: *ACS Appl Mater Interfaces.* 9.11 (2017), pp. 10136–10147. DOI: 10.1021/acsami.7b00443. URL: https://pmc.ncbi.nlm.nih.gov/articles/PMC5364429/?.

[64] Milad Haghighi et al. "Effect of Graphene Nanosheets Content on Microstructure and Mechanical Properties of Titanium Matrix Composite Produced by Cold Pressing and Sintering". In: *Nanomaterials* 8.12 (2018). ISSN: 2079-4991. DOI: 10.3390/nano8121024. URL: https://www.mdpi.com/2079-4991/8/12/1024.

[65] Elisa Torresani, Gloria Ischia, and Alberto Molinari. "Localized Defects in Cold Die-Compacted Metal Powders". In: *Journal of Manufacturing and Materials Processing* 6.6 (2022), p. 155. DOI: 10.3390/jmmp6060155. URL: https://www.mdpi.com/2504-4494/6/6/155.

[66] Copper Development Association. *Copper Powder Consolidation Techniques.* https://www.copper.org/resources/properties/129_6/consolidation.html. Accessed: 2026-06-18.

[67] Min Yi et al. "Modeling and simulation of sintering process across scales". In: *arXiv preprint arXiv:2211.00821* (2022). DOI: 10.48550/arXiv.2211.00821. URL: https://arxiv.org/abs/2211.00821.